Title:

Notch controls the cell cycle to define leader versus follower identities during collective cell migration.

Authors:

Zain Alhashem[1], Dylan Feldner-Busztin[2], Christopher Revell[2], Macarena Alvarez-Garcillan Portillo[1], Karen Camargo-Sosa[6], Joanna Richardson[1], Manuel Rocha[4], Anton Gauert[1], Tatianna Corbeaux[1], Martina Milanetto[7], Francesco Argenton[7], Natascia Tiso[7], Robert N Kelsh[6], Victoria E Prince[4, 5], Katie Bentley[2, 3, *] and Claudia Linker[1*].

Affiliations:

1: Randall Centre for Cell and Molecular Biophysics, Guy's Campus, King's College London, London, UK

2: Cellular Adaptive Behaviour Lab, Francis Crick Institute, London, UK.

3: Department of Informatics, King's College London, London, UK.

4: Committee on Development, Regeneration and Stem Cell Biology, The University of Chicago, Chicago, Illinois.

5: Department of Organismal Biology and Anatomy, The University of Chicago, Chicago, Illinois.6: Department of Biology & Biochemistry, University of Bath, Bath, UK.

7: Department of Biology, University of Padova, Padova, Italy.

*: Co corresponding authors: claudia.linker@kcl.ac.uk and katie.bentley@kcl.ac.uk

SUMMARY:

Coordination of cell proliferation and migration is fundamental for life, and its dysregulation has catastrophic consequences, such as cancer. How cell cycle progression affects migration, and vice-versa, remains largely unknown. We address these questions by combining in-silico modelling and in vivo experimentation in the zebrafish Trunk Neural Crest (TNC). TNC migrate collectively, forming chains with a leader cell directing the movement of trailing followers. We show that the acquisition of migratory identity is autonomously controlled by Notch signalling in TNC. High Notch activity defines leaders, while low Notch determines followers. Moreover, cell cycle progression is required for TNC migration and is regulated by Notch. Cells with low Notch activity stay longer in G_1 and become followers, while leaders with high Notch activity quickly undergo G_1/S transition and remain in S-phase longer. In conclusion, TNC migratory identities are defined through the interaction of Notch signalling and cell cycle progression.

KEY WORDS:

Collective cell migration, neural crest, Notch, cell cycle, zebrafish, agent-based modelling.

INTRODUCTION:

The harmonious coupling of cell proliferation with migration is fundamental for the normal growth and homeostasis of multicellular organisms. A prominent consequence of the dysregulation of these processes is cancer. Uncontrolled cell proliferation leads to primary tumours, and the acquisition of migratory capacities leads to the formation of secondary tumours, the most common cause of cancer deaths. Metastatic cells can migrate collectively, which endows them with more aggressive behaviours (Nagai et al., 2020). Collective cell migration refers to the movement of a group of cells that maintain contact and read guidance cues cooperatively (Rørth, 2009). This mechanism has been studied in several contexts, such as wound healing, angiogenesis, and neural crest migration. However, how cell proliferation impacts collective cell migration, and *vice versa*, remains largely unknown. The molecular signals that may couple these two fundamental processes remain equally unclear.

The NC is a mesenchymal cell population that arises early in development and migrates throughout the body giving rise to a variety of cell types (neurons, glia, pigment cells, etc.). The NC's stereotypical migratory behaviour (Gammill and Roffers-Agarwal, 2010) and similarity to metastatic cells (Maguire et al., 2015) makes this cell type an ideal model to study the mechanisms of collective cell migration in vivo. Our previous work has shown that zebrafish trunk neural crest (TNC) migrate collectively forming single file chains (Richardson et al., 2016). One cell at the front of the chain, the leader, is the only cell capable of instructing directionality to the group, while follower cells trail the leader. This division of roles into leaders and followers has been observed in other collectively migrating systems (Theveneau and Linker, 2017). Moreover, histopathological studies from cancer samples and cell lines show clear morphological and molecular differences between the invasive front, leaders, and the lagging cells, followers (Pandya et al., 2017). One outstanding question from these studies is what are the signals that determine leader versus follower migratory identities?

Notch signalling is a cell-cell communication pathway that directly translates receptor activation at the membrane into gene expression changes. Notch receptors are activated by membrane-bound ligands of the Delta/Serrate/Lag2 family. Upon ligand binding, Notch receptors are cleaved by γ-secretases releasing its intracellular domain (NICD). Subsequently, NICD translocates to the nucleus, binds the CBF1/Su(H)/Lag-1 complex and initiates transcription (Bray, 2016). Among the direct Notch targets are members of the Hes gene family, which encode transcriptional repressors able to antagonize the expression of specific cell fate determinants and Notch ligands, generating a negative feedback loop in which cells with high Notch receptor activity downregulate the expression of Notch ligands, and cannot activate the pathway in their neighbours. Hence, adjacent cells interacting through the Notch pathway typically end up with either low or high levels of Notch activity and adopt distinct fates, a mechanism known as lateral inhibition (Lewis, 1998). Interestingly, Notch signalling has also been implicated in cell migration (Giniger, 1998; Leslie

et al., 2007; Timmerman, 2004) and promotes invasive behaviours during cancer progression (Reichrath and Reichrath, 2012). Furthermore, lateral inhibition is implicated in the allocation of migratory identities during angiogenesis (Phng and Gerhardt, 2009), trachea formation in *Drosophila* (Caussinus et al., 2008) and in cell culture (Riahi et al., 2015). Whether Notch signalling plays a similar role in the context of mesenchymal cell migration is unknown. Notch signalling is required for NC induction (Cornell and Eisen, 2005) and its components and activity remain present in migrating NC (Liu et al., 2015; Rios et al., 2011). Nevertheless, the role of Notch during NC migration remains unclear. Cardiac NC are reported to develop normally under lack of Notch signalling (High et al., 2007). However, using different genetic tools, it has been shown that both gain and loss of Notch function led to the lack of NC derivatives (Mead and Yutzey, 2012). Moreover, in *Xenopus* the loss of Notch effectors leads to aberrant NC migration (Vega-López et al., 2015).

The Notch pathway has not only been implicated in cell fate allocation, but it is also important for cell proliferation. Depending on the context, Notch can inhibit or promote cell cycle progression (Campos et al., 2002; Carlson et al., 2008; Devgan et al., 2005; Fang et al., 2017; Georgia et al., 2006; Mammucari et al., 2005; Nguyen et al., 2006; Nicoli et al., 2012; Noseda et al., 2004; Ohnuma et al., 1999; Park et al., 2005; Patel et al., 2016; Rangarajan et al., 2001; Riccio et al., 2008; Zalc et al., 2014). Indeed, Notch target genes include important cell cycle regulators such as CyclinD1, p21 and MYC (Campa et al., 2008; Guo et al., 2009; Joshi et al., 2009; Palomero et al., 2006; Ronchini and Capobianco, 2001).

Using a combination of in vivo and in-silico approaches we have established that differences in Notch activity between premigratory TNC select the leader cell. Cells with high levels of Notch signalling adopt a leader identity, while cells that lack Notch activity become followers. Our data show that a single progenitor cell in the premigratory area divides asymmetrically giving rise to a large prospective leader and smaller follower cell. We propose that this original small asymmetry generates differences in Notch activity between TNC that are thereafter enhanced by cell-cell communication through Notch lateral inhibition. Differences in Notch activity in turn drive distinct cell cycle progression patterns and regulate the expression of *phox2bb*. Leader cells undergo the G_1/S transition faster and remain in S-phase for longer than follower cells. Moreover, continuous progression through the cell cycle is required for TNC migration. Taken together, our results support a model in which the interaction between Notch and the cell cycle defines leader and follower migratory behaviours.

RESULTS:

Notch signalling is required for TNC migration.

NC cells are induced at the border of the neural plate early during development. The prospective NC expresses Notch components, and Notch activity is required for NC induction (Cornell and Eisen, 2005). Our analysis reveals that Notch components remain expressed in NC after induction,

136 suggesting Notch signalling may also be involved in later aspects of NC
137 development (Figure 1-figure supplement 1). Moreover, analysis of the Notch
138 activity reporter line 12xNER:egpf (Moro et al., 2013), shows that Notch
139 signalling levels vary widely between premigratory TNC (Figure 1) suggesting
140 that Notch may play a role after TNC induction. To explore the role of Notch in
141 TNC development, we first aimed to define the stage at which NC induction
142 becomes independent of Notch signalling. To this end, we treated embryos with
143 the γ-secretase inhibitor DAPT (Richter et al., 2017) and assessed expression of
144 NC marker. Our results showed that Notch inhibition impairs TNC induction up to
145 11hpf (Figure 2), and confirmed previous reports that induction of the cranial
146 and vagal NC populations is independent of Notch signalling (Cornell and Eisen,
147 2000). Next, we analysed the effect of Notch inhibition at 12hpf on the
148 development of TNC derivatives. We found a reduction in all TNC derivatives
149 (neurons, glia, and pigment cells; Figure 3A-F) upon Notch inhibition, suggesting
150 that Notch activity is important in a process subsequent to induction, yet prior to
151 differentiation. We next explored whether TNC migration is affected by Notch
152 inhibition. Analysis of *crestin* expression showed a reduction in the number of
153 TNC cell chains formed and in their ventral advance upon DAPT treatment
154 (Figure 3G-J), which likely explains the lack of TNC derivatives at later stages.
155 We then asked whether these results are due to a delay or a halt of migration.
156 To this end, embryos were treated with DAPT from 12hpf for 6 to 12h and
157 processed for *crestin* expression. Decreased numbers of migratory chains were
158 observed at all timepoints, but as embryos developed new chains were formed,
159 indicating that the blockade of Notch signalling delays TNC migration (Figure
160 3K). Comparable results were obtained by inhibiting Notch genetically in
161 embryos where the dominant-negative form of Suppressor of Hairless is under
162 the control of a heat shock element (Latimer et al., 2005; hs:dnSu(H); Figure
163 3L). We reasoned that if Notch inhibition delays the onset of TNC migration, its
164 overactivation might lead to TNC migrating earlier leading to an increased
165 number of chains. To test this, we induced NICD expression in all tissues by heat
166 shock of hs:Gal4;UAS:NICD embryos (Scheer and Campos-Ortega, 1999). To
167 our surprise, Notch gain and loss of function resulted in almost identical
168 phenotypes, both showing a similar reduction of TNC chain numbers (Figure 3L).
169 Taken together, these results show that precise regulation of Notch signalling
170 levels is required for TNC migration.
171
172 **In vivo Notch activity allocates TNC migratory identity.**
173 Interestingly, Notch signalling is required during collective migration to
174 define distinct identities (Phng and Gerhardt, 2009; Caussinus et al., 2008; Riahi
175 et al., 2015) . To test whether Notch plays a similar role in TNC migration we
176 performed live-imaging analysis of TNC migration under lack (inhibition and loss
177 of function, LOF) or overactivation (gain of function, GOF) of Notch signalling
178 (Figure 4; Figure 4-video 1 and 2). Our previous work defined a leader as the
179 cell that retains the front position of the chain throughout migration, advancing
180 faster and in a more directional manner than followers (Richardson et al., 2016).

181 Under Notch inhibition (treatment with γ-secretase inhibitor Compound E;
182 Richter et al., 2017) TNC remain motile with a single cell initiating the
183 movement of the chain, but in contrast to control treatment (DMSO) the leader
184 cell is unable to retain the front position and is overtaken by one or several
185 followers (Figure 4A and C, and 5A-B; Figure 4-video 1). The overtaking follower
186 cell, in turn, is not always able to retain the front position and can be overtaken
187 by cells further behind in the chain. This loss of group coherence corresponds
188 with a reduction in ventral advance, with most leader cells unable to move
189 beyond the neural tube/notochord boundary (NT/not; Figure 4C and 5A and C).
190 This behaviour leads to an accumulation of cells at the NT/not, where some cells
191 repolarise moving anterior or posteriorly and crossing the somite boundary and,
192 in some cases, joining adjacent chains. Analysis of single cell tracking showed
193 that under Notch inhibition leader cells also have decreased speed and
194 directionality (Figure 5D-E). Similar results were observed when Notch inhibition
195 was achieved genetically by driving overexpression of dnSu(H) through heat
196 shock in the entire embryo (not shown; hs:dnSu(H) line). Together, these
197 results strongly suggest that upon lack of Notch signalling the TNC population is
198 formed solely by follower cells that are unable to coordinate the movement of
199 the group. Nevertheless, Notch signalling is important for the development of
200 tissues surrounding TNC that act as a substrate for migration, raising the
201 possibility that Notch signalling does not act cell autonomously in TNC and
202 instead the phenotypes observed are simply the consequence of somite and/or
203 neural tube malformations. However, this appears unlikely, as somite
204 development (formation, patterning, and differentiation) and neuron formation
205 are not affected by Notch inhibition at the axial level analysed (Figure 4-figure
206 supplement 1). Next, we directly tested whether Notch signalling is
207 autonomously required in TNC by inhibiting Notch activity exclusively in NC at
208 the time of migration. To this end, we generated a new UAS:dnSu(H) line and
209 crossed it with Sox10:Kalt4 fish (Alhashem et al., 2021). In the resultant
210 embryos all NC express Gal4 fused to the oestrogen receptor binding region
211 (Gal4-ER) and are fluorescently labelled by nuclear-RFP. Under normal
212 conditions, Gal4-ER is maintained inactive in the cytoplasm, whilst upon addition
213 of tamoxifen, Gal4-ER is translocated to the nucleus activating transcription from
214 the UAS:dnSu(H) transgene (Figure 4-figure supplement 2). We found that
215 autonomous inhibition of Notch signalling in NC phenocopies the chemical
216 inhibition. Leader cells are unable to retain the front position, being overtaken
217 by followers, and ventral advance is reduced with cells accumulating at the
218 NT/not boundary (Figure 4D and 5A-C; Figure 4-video 2). Moreover, leader cells
219 adopt followers' migratory parameters, showing decreased speed and
220 directionality (Figure 5D-E), confirming that Notch activity is autonomously
221 required in TNC for identity allocation, and suggest that in the absence of Notch
222 signalling a homogenous group of followers is established. In view of these
223 results, we hypothesised that a homogeneous group of leaders would be formed
224 upon Notch overactivation. Using a similar strategy, Notch overactivation was
225 induced in the whole embryo (not shown, hs:Gal4;UAS:NICD; Scheer and

226 Campos-Ortega, 1999), or exclusively in NC (Sox10:Kalt4;UAS:NICD) and
227 migration was analysed by live-imaging. Similar results were obtained in both
228 experimental conditions: group coherence is lost, leader cells are overtaken by
229 followers, and ventral advance is impaired (Figure 4F and 5A-C; Figure 4-video
230 2). Interestingly, in Notch GOF conditions follower cells adopt leaders'
231 characteristics, moving with increased speed, but all cells in the chain follow less
232 directional trajectories, which hinders the ventral advance of the group (Figure
233 5D-E), indicating that all cells in the chain migrate as leaders. Next, we tested
234 whether the behavioural changes observed upon Notch alterations were mirrored
235 by molecular changes by using the leader marker *phox2bb*. In control conditions
236 *phox2bb* transcripts are highly enriched in the leader cells from early stages of
237 migration (Figure 6A-B and G; Alhashem et al., 2022). Consistent with
238 expectations, upon Notch overactivation *phox2bb* is expressed by all the cells in
239 the chain (Figure 6C-D and G), while its expression is absent when Notch is
240 inhibited (Figure 6E-F and G). These data show that Notch activity controls
241 *phox2bb* expression and allocates TNC migratory identity.
242 In summary, our in vivo and molecular data show that Notch signalling is
243 required autonomously in TNC for migratory identity allocation. TNC with high
244 levels of Notch express *phox2bb* and become leaders, while cells with low Notch
245 activity migrate as followers. Alterations of Notch signalling leads to a
246 homogeneous TNC group with a single migratory identity that is unable to
247 undergo collective migration. Taken together these data suggest Notch lateral
248 inhibition as the mechanism responsible for TNC migratory identity acquisition.
249
250 **In-silico modelling predicts that more than one leader is required for**
251 **TNC migration..**
252 Our in vivo analysis show that upon both Notch inhibition and overactivation
253 TNC are unable to undergo collective migration due to lack of group coherence.
254 On the other hand, our molecular analysis show that upon Notch inhibition an
255 all-followers group is established, while Notch overactivation leads to the
256 formation of an all-leaders group. To gain a better understanding of these
257 paradoxical results we took an in-silico approach, developing a discrete element
258 model of TNC migration. Cells were simulated as 2D particles moving into a
259 constrained space and endowed with intrinsic motility. Four variables control cell
260 movement in the model: contact inhibition of locomotion (CIL) and co-attraction
261 (co-A) define movement directionality and group cohesion, while volume
262 exclusion regulates cell overlap, intuitively understood as cell size, while a noise
263 element (zeta) was added to the cell's trajectory (Figure 7A). A multi-objective
264 scoring system, based on in vivo measurements, was developed to evaluate how
265 close simulations with different underlying mechanisms matched chain
266 behaviours. The scores were: 1. chain cohesion, a maximum distance of 57μm is
267 allowed between adjacent cells, 2. single file migration for at least 80% of the
268 simulation 3. followers undergo rearrangements, while 4. leaders retain the front
269 position, and 5. the chain should advance to the end of the migratory path
270 (Figure 7B). Using this analysis and a parsimonious modelling approach, we

271 attempted to match in vivo TNC migration with the simplest form of the model,
272 only adding complexity incrementally in an effort to find the minimal set of
273 predicted mechanisms required. We first simulated chains composed of
274 homogeneous cells and systematically covaried all parameters. We found no
275 parameter combination able to match all scores, confirming our previous findings
276 that cell heterogeneity is required for TNC migration (Figure 7C; Richardson et
277 al., 2016). Evidence from other systems (Astin et al., 2010; Bentley et al.,
278 2014; Parkinson and Edwards, 1978; Theveneau and Mayor, 2013) led us to
279 hypothesise that differences in the CIL response between cells may be at play.
280 Thus, we simulated chains in which only cells of different identities present CIL
281 (Diff CIL; Figure 7A). These simulations match several scores, but chains are
282 unable to reach the end of the migratory path (Figure 7C; Figure 4-video 3).
283 Next, we varied Diff CIL intensity, co-A and cell size (volume exclusion) for
284 leader cells. Interestingly, the model is only able to recapitulate control
285 conditions when the difference between leaders and follower is maximal for all
286 variables. Nevertheless, it is unable to recapitulate Notch GOF and LOF
287 phenotypes (Figure 7C). Our previous results show that differences in Notch
288 signalling establish migratory identities, suggesting that lateral inhibition may be
289 the mechanism at play. To explore whether different outcomes of lateral
290 inhibition may allow the model to simulate Notch altered conditions (GOF and
291 LOF), different ratios of leader/follower cells were simulated. We first tested a
292 1:1 ratio, surprisingly this chain architecture over-migrates, moving beyond the
293 end of the pathway (Figure 7C; Figure 4-video 3). Interestingly, we found that
294 several parameter combinations from the 1:2 and 1:3 leader/follower ratios
295 were able to recapitulate in vivo control condition, as well as the loss of group
296 coherence and ventral advance observed in Notch GOF (all leader simulation)
297 and LOF (all follower simulation; Figure 4B, E and G, and Figure 5; Figure 4-
298 video 3). In these simulations, the six parameter combinations that match all in
299 vivo scores had followers at the low setting, while leaders' CIL intensity took
300 medium or high values, cell size took medium or low values and co-attraction
301 took all levels. Nevertheless, all these parameter combinations endow the leader
302 with enhanced migratory behaviour.
303 Next, we used a linear discriminant analysis (LDA) to study which of the
304 model parameters bear most weight in the definition of leader and follower
305 identity. LDA is a dimensionality reduction method that projects the data onto a
306 lower dimensional space minimizing the variation within classes (e.g. between
307 leaders) and maximizing the variation between classes (leaders versus
308 followers), allowing the hierarchical ordering of the factors that best explain the
309 class separation. First, we used the in vivo data to determine whether leaders
310 and followers were properly separated by LDA. A visual inspection of the data
311 makes clear that LDA works well to classify migratory identities (Figure 7D).
312 Moreover, the LDA analysis shows that ventral distance is the most important
313 variable separating leaders from followers, with speed and directionality playing
314 a less dominant role (Figure 7E). Next, we used this method to assess the
315 importance of each of the model parameters. CIL intensity appears to be the

316 parameter that most differ between leader and follower cells, while
317 heterogeneity in the other parameters is not essential (Figure 7F). Taken
318 together, the in-silico data confirms our previous conclusion that TNC chains are
319 a heterogeneous group. Remarkably, it also predicts CIL intensity to be the most
320 important distinction between leaders and followers. Finally, the model
321 anticipates that TNC chains are formed of leaders and followers in a 1:2 or 1:3
322 ratio.
323
324 **Leader cells arise from the asymmetric division of a progenitor cell.**
325 Cell size is a prominent characteristic distinguishing leader from follower
326 cells. Leaders are almost twice as big as followers during migration and this
327 difference is evident before migration initiation (Richardson et al., 2016),
328 suggesting that size disparity arises at birth or shortly thereafter. Interestingly,
329 differential cell size emerged as an important parameter in our *in-silico* analysis,
330 contributing to more realistic leader/follower coordination behaviours. To
331 understand the origin of these size differences we investigated whether leader
332 and follower cells share a common progenitor, and at which point differences in
333 size become apparent. To this end we imaged FoxD3:mCherry;H2aFVA:H2a-GFP
334 embryos. The FoxD3:mCherry reporter (Hochgreb-Hägele and Bronner, 2013;
335 Lukoseviciute et al., 2018) labels NC from early stages and allows us to define
336 TNC identity at later stages by their migratory position. Moreover, the nuclear
337 marker H2aFVA:H2a-GFP (Pauls et al., 2001) was used to track single cells and
338 their divisions. Tracking analysis shows that the asymmetric division of a single
339 progenitor cell in each body segment gives rise to a larger cell that becomes a
340 leader (102 ± 20 μm^2), and a smaller sibling that migrates as follower (72 ± 9
341 μm^2; Figure 8A and B; Figure 8-video 1). In contrast, all other progenitors divide
342 symmetrically giving rise to two follower cells (87 ± 27 μm^2; Figure 8C and D).
343 We also noticed that the leader progenitors' divisions are spatially restricted to
344 the anterior quarter of the premigratory area in each segment, while the
345 followers' progenitor divisions take place across the premigratory area (Figure
346 8E).
347 We then reasoned that leader cells, being bigger, may undergo the next
348 division in a shorter time span than follower cells and in consequence, mitotic
349 figures would be observed at different, but consistent, positions in their
350 trajectory. Indeed, we found two different patterns of divisions in respect to
351 migration: i) cells that first Divide and then Migrate (D→M), or ii) cells that first
352 Migrate and then Divide (M→D; Figure 8F-G; Figure 8-video 2). Interestingly, we
353 found that the patterns of cell division correlate with cell identity. Most leader
354 cells divide during migration (M→D: 86%), while the bulk of follower cells divide
355 before migration initiation (D→M: 90%, Figure 8H). These patterns result in
356 leader and follower cells dividing at distinct positions, 74% of leaders divide at
357 the NT/not boundary (65.3 ± 9.6 μm), while 85% of followers divide mostly
358 within the premigratory area or in the dorsal-most region of the somite (42 ±
359 12.4 μm; Figure 8I). Together, these results show that leader cells arise from
360 the asymmetric division of a progenitor. Thereafter, leader and follower cells

361 show distinct locations and patterns of division, suggesting that leaders and
362 followers progress asynchronously through the cell cycle, which may influence
363 their migratory behaviour.
364
365 **Cell cycle progression is required for TNC migration.**
366 To test the role of cell cycle progression in TNC migration directly, we used
367 inhibitory drugs. The S-phase inhibitor Aphidicolin blocks over 94.7 ± 4.5% of
368 mitotic figures after 3h of treatment, while the G2/M inhibitor Genistein prevents
369 90 ± 10% of divisions within 6h, but neither treatment affects NC induction
370 (Figure 9-figure supplement 1). Inhibition of cell cycle progression by either of
371 the treatments resulted in reduced numbers of migratory chains and decreased
372 ventral advance (Control 19 ± 2, Genistein 10 ± 3, Aphidicolin 6 ± 2 chains;
373 Figure 9A-H). This result was not due to the loss of cell motility, as premigratory
374 TNC cells actively extend protrusions and move along the antero-posterior axis
375 but are unable to migrate ventrally (Figure 9-video 1). Importantly, these effects
376 were not a consequence of cell death or the permanent impairment of motility,
377 as TNC re-initiate migration and form new chains upon drug withdrawal (Figure
378 9G and H); showing that active cell cycle progression is required for migration.
379 Next, we directly analysed TNC cell cycle progression in vivo. To this end, we
380 imaged Sox10:FUCCI embryos (Rajan et al., 2018), in which TNC nuclei are RFP-
381 labelled during G_1 and GFP-labelled during S and G_2. Tracking analysis show
382 differential cell cycle progression, with most leader cells initiating migration in S-
383 phase (79%), while followers start movement during G_1 (77%; Figure 9I and J;
384 Figure 9-video 2). These results show that cell cycle progression is required for
385 migration and that leader and follower cells initiate movement at different points
386 of the cell cycle, suggesting an intimate connection between cell growth and
387 movement.
388
389 **Leader and follower cells progress through the cell cycle at different**
390 **rates.**
391 Next, we studied TNC cell cycle progression in detail. First, we asked
392 whether leaders and followers differ in the total length of their cell cycle.
393 Measurements of the time span between two consecutive mitoses showed no
394 significant differences in the total length of the cell cycle between leaders and
395 followers (13.6 ± 1.2 and 13.3 ± 1.4 h respectively; Figure 10B). Next, we
396 examined the length of each phase of the cell cycle by imaging the characteristic
397 nuclear labelling pattern of the PCNA-GFP fusion protein (Leung et al., 2012).
398 Sox10:Kalt4 embryos, in which all NC can be recognized by nuclear RFP
399 expression, were injected with PCNA-GFP mRNA and live imaging was
400 performed. PCNA-GFP shows uniform nuclear GFP labelling during G_1, intense
401 fluorescent nuclear puncta characterise the S-phase, these puncta dissipate
402 during G_2 restoring homogeneous nuclear fluorescence, at the onset of mitosis
403 PCNA is degraded and TNC are recognized solely by nuclear RFP (Figure 10A;
404 Figure 10-video 1). In these embryos, leader cells initiate migration during S-
405 phase and followers in G_1, confirming our FUCCI results and establishing that

406 PCNA overexpression does not introduce artefacts to cell cycle progression
407 (Figure 10-figure supplement 1). Using this tool, we measured the length of the
408 cell cycle phases in TNC. We found striking differences in the time spent in G_1-
409 and S-phase between leader and follower cells. Leaders present a short G_1 (3.2
410 ± 0.6h) but remain for twice as long in S-phase (8.7 ± 1.3h). Followers, on the
411 other hand present the opposite distribution, remaining for twice as long in G_1
412 (7.4 ± 2.7h) than in S-phase (4.6 ± 2.8h; Figure 10C-D). No significant
413 differences were observed in the length of G_2 (leaders 1.6 ± 0.4 h; followers 1.5
414 ± 0.3h) or M (leaders 0.6 ± 0.1h; followers 0.5 ± 0.1h). These data show that
415 leader and follower cells present marked differences in the length of G_1- and S-
416 phase, suggesting that cell cycle progression may regulate their migratory
417 behaviour.
418
419 **Notch signalling regulates TNC cell cycle progression.**
420 Our data show that Notch signalling allocates leader and follower identities,
421 that cell cycle progression is necessary for TNC migration, and that leader and
422 follower cells progress through the cell cycle at different rates. Does Notch
423 signalling regulate cell cycle progression, thus differentiating leader from
424 follower cells? To investigate this question, we measured the total length of the
425 cell cycle and the length of each phase under control and Notch-inhibited
426 conditions. Neither the total cell cycle length (Figure 11A), nor the number of
427 TNC (Figure 9-figure supplement 1) were affected by alterations of Notch
428 signalling. Remarkably, we found significant differences in the length of G_1- and
429 S-phase upon Notch inhibition. Leader cells lose their characteristic cell cycle
430 progression pattern and behave as followers, with a long G_1 and a short S-phase
431 (Figure 11B). Furthermore, Notch inhibition abolishes the size difference
432 between migratory leader and follower cells, with all cells presenting the average
433 follower's area (Figure 11C-D). These data show that Notch activity defines TNC
434 migratory identity by regulating cell cycle progression, cells with low Notch
435 activity remain for longer in G_1 behaving as followers. Interestingly, we noticed
436 that Notch inhibition also changes the cell cycle behaviour of the followers'
437 population. While the followers' average length of cell cycle phases is not
438 altered, the dispersion of this population is significantly reduced, with standard
439 deviations cut almost by half (from 2.7h to 1.42h for G_1 and from 2.8h to 1.38h
440 for S; Figure 11B). This prompted us to analyse the frequency distribution of cell
441 cycle phases length. In control conditions, leader cells show a normal distribution
442 with a single peak for G_1- and S-phase, as expected for a homogeneous
443 population. Followers, on the other hand, present a bimodal distribution, with
444 the smaller peak coinciding with that of leader cells, and accounting for 26% of
445 followers in G_1- and 31% in S-phase (Figure 11E and F). Strikingly, these results
446 fulfil the predictions of our in-silico model that best recapitulates TNC migration
447 when chains are composed of leaders and followers in a 1:2 or 1:3 ratios.
448 Furthermore, upon Notch inhibition the bimodal distribution of the follower
449 population is lost, with all cells grouped at the major mean (Figure 11G and H).
450 Consistent with these data, closer analysis (at higher magnification) of normal

451 *phox2bb* expression shows increased expression followers in position three in
452 addition to that in leaders (Figure 11I-N). Taken all together, our data
453 demonstrate that the levels of Notch activity in TNC allocate migratory identity
454 by controlling cell cycle progression and that migratory chains are formed of one
455 leader cell for every three followers.
456
457 **DISCUSSION:**
458 Collective migration plays an important role in embryogenesis, wound
459 healing, and cancer. The acquisition of specific migratory identities has proven
460 fundamental to angiogenesis, trachea development in Drosophila and cancer
461 metastasis. TNC migrate collectively, forming chains with a leader cell at the
462 front of the group that direct the migration, while follower cells form the body of
463 the chain that trails the leaders. TNC leader and follower identities are
464 established before migration initiation and remain fixed thereafter (Richardson et
465 al., 2016). Herein, we have addressed the mechanism that establishes leader
466 and follower identities and can propose the following model (Figure 12): A)
467 premigratory TNC progenitors arise at the dorsal part of the neural tube. The
468 leader's progenitor divides asymmetrically giving rise to a large prospective
469 leader cell and a small sibling that migrates as a follower. Other progenitors
470 divide symmetrically giving rise to follower cells. B) Interactions via Notch
471 signalling results in the prospective leader cell accumulating higher levels of
472 Notch activity, which induces *phox2bb* expression. C) The combination of high
473 Notch activity and a larger cell size prompts the prospective leader cell to rapidly
474 undergo the G_1/S transition, entering S-phase and initiating migration earlier
475 than its follower siblings, which are smaller and initiate migration whilst in G_1. D)
476 Premigratory cells that have not been in contact with the prospective leader cell,
477 or that have lost contact with it due to its ventral advance, maintain
478 communication with surrounding premigratory TNC through Notch and undergo
479 a new round of leader cell selection. This working model of TNC migration is
480 supported by both our experimental data and our in-silico modeling, and
481 provides a useful conceptual framework for future studies to build upon.
482 Notch signalling is a seemingly simple pathway that directly transduces
483 receptor activation into changes in gene expression. Nevertheless, its outcomes
484 in terms of cellular patterning are very diverse, from the generation of gene
485 expression boundaries to temporal oscillations, or from the induction of similar
486 fates in neighbouring cells to forcing adjacent cells into alternative fates. The
487 latter function, known as lateral inhibition, is characterised by an intercellular
488 negative feedback loop regulating the expression of Notch ligands. The
489 activation of the Notch receptor in a "signal-receiving" cell leads to the
490 downregulation of Notch ligands expression, making it less able to act as a
491 "signal-sending" cell. The signature 2D patterning outcome of lateral inhibition is
492 a mosaic of signal-sending cells with low Notch activity, surrounded by signal-
493 receiving cells with high Notch levels. This is the case during the selection of
494 sensory organ precursor cells in the epidermis of *Drosophila* (Lewis, 1998), or
495 the formation of the mosaic of hair cells and supporting cells in the sensory

496 organs of the inner ear (Daudet and Żak, 2020). In general, however, lateral
497 inhibition operates among cells subjected to extensive rearrangements and its
498 patterning outcome is not a salt-and-pepper mosaic of cells (Bocci et al., 2020).
499 For example, during angiogenesis, cells with low Notch signalling become tip or
500 leaders, while cells with high Notch activity differentiate as stalk or followers
501 (Phng and Gerhardt, 2009). In this context, leaders are interspersed with
502 various numbers of followers. Several models have been proposed to explain
503 how signal-sending (leader/tip) cells can exert a long-lasting or long-range
504 inhibition on signal-receiving (follower/stalk) cells. These take into account the
505 modulation of Notch signalling that arise from heterogeneity in Notch receptor
506 levels, tension, Notch-regulators and interaction with other pathways (Bentley
507 and Chakravartula, 2017; Hadjivasiliou et al., 2019; Koon et al., 2018; Kur et
508 al., 2016; Venkatraman et al., 2016). Our data show that TNC deviate from the
509 classical mosaic pattern, forming chains with one leader every two or three
510 followers. Further studies will be required to define whether the aforementioned
511 mechanisms are responsible for this architecture.
512 In the case of the TNC, however, the most striking divergence from the
513 classic lateral inhibition model (or indeed angiogenesis) is the fact that the
514 leader cell identity is associated with higher intrinsic Notch activity. In other
515 words, there are more signal-sending cells than signal-receiving cells. This
516 apparent inversion in the ratio of the cell types produced is surprising.
517 Explanation of this conundrum may arise from the fact that Notch lateral
518 inhibition, dynamics and outcomes, can be modulated by "cis-inhibition", a
519 process whereby Notch ligands cell-autonomously interfere with the activation of
520 Notch receptors (Bray, 2016; del Álamo et al., 2011). Computational models
521 show that an increase in the strength of cis-inhibition can result in the inversion
522 of the salt and pepper pattern (signal-sending to signal-receiving cells ratio),
523 with the production of one cell with high Notch activity for every three cells with
524 low Notch levels (Formosa-Jordan and Ibañes, 2014), a scenario that is
525 congruent with the leader/follower ratio we observe in TNC. The detailed
526 dynamics of lateral inhibition and whether cis-inhibition is at work in TNC remain
527 to be investigated and will require direct visualisation at the single cell level of
528 Notch activity in live embryos.
529 Our data show that active progression through the cell cycle is required for
530 TNC migration. This is consistent with studies in chicken embryos, showing that
531 progression through G_1/S is required for TNC delamination, and that NC continue
532 cycling as they migrate (Burstyn-Cohen and Kalcheim, 2002; Theveneau et al.,
533 2007). Our data extend these findings by showing that leader and follower cells
534 progress through the cell cycle at different rates. Leader cells, which are larger
535 and more motile, initiate migration in S-phase and spend twice as long in this
536 phase as followers. It is possible that these differences arise from the fact that
537 leaders are larger than followers. It has been shown that the timing of G_1/S
538 transition depends on cell size and the dilution of the nuclear retinoblastoma
539 protein (Zatulovskiy and Skotheim, 2020). Due to the larger volume of their
540 cytoplasm leader cells could be primed for a rapid G1/S phase transition. The

541 initiation of S-phase may in turn enhance leaders' migratory characteristics
542 through the interaction of cyclins and Cyclin/CDK inhibitors (CDKI) with small
543 GTPases. Cyclin B and D, have been shown to phosphorylate cytoskeleton
544 regulators, resulting in increased cell migration and tumour invasion (Blethrow
545 et al., 2008; Chen et al., 2020; Chi et al., 2008; Hirota et al., 2000; Li et al.,
546 2006; Manes et al., 2003; Song et al., 2008; Zhong et al., 2010). Furthermore,
547 Rac1 activity, which is required for migration, oscillates during the cell cycle
548 being highest at S-phase when cells are most invasive (Kagawa et al., 2013;
549 Walmod et al., 2004). CDKIs, on the other hand, interact with RhoA and ROCK
550 enhancing motility (Bendris et al., 2015; Creff and Besson, 2020; Yoon et al.,
551 2012). Interestingly, enhanced motility increases actin branching, which in turn
552 can accelerate the G_1/S transition (Molinie et al., 2019). These factors could
553 therefore generate a positive feedback loop in which slightly larger leader cells
554 are prone to undergo the G_1/S transition, in turn the activation of S-phase
555 cyclins and CDKIs may enhance motility reinforcing S-phase initiation.
556 Our data also show that TNC cell cycle progression is under the control of
557 Notch signalling. Upon Notch inhibition, all TNC present cell cycle phase lengths
558 typical of follower cells. Notch has been shown to regulate cell cycle in a context-
559 dependent manner. Depending on the cell type, Notch can regulate cell cycle
560 through the transcriptional induction of Cyclin A and D, and the inhibition of
561 CDKIs (Campa et al., 2008; Dabral et al., 2016; Ridgway et al., 2006; Rizzo et
562 al., 2008; Rowan et al., 2008). Conversely, cell cycle progression can impact on
563 Notch signalling. Notch activity is enhanced at the G_1/S transition, while cells
564 become refractory to Notch during G_2/M (Ambros, 1999; Carrieri et al., 2019;
565 Hunter et al., 2016; Nusser-Stein et al., 2012). Hence, the combination of large
566 volumes and higher Notch activity levels could act synergistically to promote
567 leaders' G_1/S transition.
568 In this study, we have uncovered new functional interactions between
569 Notch signalling, cell cycle dynamics, and the migratory behaviour of leader and
570 follower cells in the TNC. These complex and intricate interactions, which remain
571 to be fully characterised at a molecular level, could apply to other cell types
572 exhibiting collective migration. For example, studies in cancer cell lines have
573 shown that activation or inhibition of Notch signalling hinders migration, similar
574 to what we observe in TNC (Konen et al., 2017), while the maintenance of
575 collective migration depends in on the regulation of cell proliferation during
576 angiogenesis (Costa et al., 2016). In view of our work, it is important to revisit
577 the assumption that migratory phenotypes are in conflict with cell cycle
578 progression (Kohrman and Matus, 2017), and consider the possible implication
579 for cancer therapies.
580
581 **ACKNOWLEDGMENTS:**
582 In memory of Julian Lewis. We are especially grateful to N. Daudet for his
583 scientific and personal support. To the KCL fish facility staff, particularly to J.
584 Glover. We are grateful to Y. Hinits and S. Wilson for sharing reagents. This
585 project was funded by MRC G1000080/1, Royal Society 2010/R1 and Wellcome

586 Trust 207630/Z/17/Z to CL; MR was supported by the Eunice Kennedy Shriver
587 National Institute of Child Health & Human Development of the National
588 Institutes of Health under awards T32HD055164 and F31HD097957. KB and DF-
589 B were supported by the Francis Crick Institute core funding from CRUK
590 (FC001751), MRC (FC001751), and Wellcome Trust (FC001751); BBSRC
591 BB/S015906/1 to RNK.
592 **DECLARATION OF INTERESTS:**
593 The authors declare no competing interests.
594
595 **MATERIALS AND METHODS:**
596 **Key Resources Table**

Key Resources Table				
Reagent type (species) or resource	**Designation**	**Source or reference**	**Identifiers**	**Additional information**
genetic reagent (Danio rerio)	Sox10:mG; Tg(-4.9sox10: Hsa.HIST1H2BJ -mCherry-2A-GLYPI-EGFP)	(Richardson et al., 2016)	ZDB-TGCONSTRCT-171205-3	
genetic reagent (Danio rerio)	Sox10:Fucci; Tg(-4.9sox10 :mAGFP-gmnn-2A-mCherry-cdt1)	(Rajan et al., 2018)	ZDB-TGCONSTRCT-190118-1	
genetic reagent (Danio rerio)	hs:dnSu(H); vu21Tg (hsp70l:XdnSu(H)-myc)	(Latimer et al., 2005)	ZDB-ALT-050519-2	
genetic reagent (Danio rerio)	hs:Gal4; kca4Tg Tg(hsp70l:Gal4)1.5kca4 (1)	(Scheer and Campos-Ortega, 1999)	ZDB-ALT-020918-6	
genetic reagent (Danio rerio)	UAS:NICD; Tg(UAS:myc-Notch1a-intra)kca3Tg	(Scheer and Campos-Ortega, 1999)	ZDB-ALT-020918-8	

genetic reagent (Danio rerio)	Tg(UAS:dnSu(H))	This paper		
genetic reagent (Danio rerio)	Sox10:Kalt4; Tg(-4.9sox10: Hsa.HIST1H2BJ -mCherry-2A-Kalt4ER)	(Alhashem et al., 2021)		
genetic reagent (Danio rerio)	Tg(h2afva:GFP) kca13	(Pauls et al., 2001)	ZDB-ALT-071217-3	
genetic reagent (Danio rerio)	Gt(FoxD3:mCherry)ct110aR	(Hochgreb-Hägele and Bronner, 2013; Lukosevicute et al., 2018)	ZDB-FISH-150901-9571	
antibody	Anti-Myosin heavy chain (Mouse Monoclonal)	Developmental Studies Hybridoma Bank	F59	IF(1:200)
antibody	Anti-Synaptotagmin 2 (Mouse Monoclonal)	Developmental Studies Hybridoma Bank	Znp1	IF(1:50)
antibody	Anti-Acetylated Tubulin (Mouse Monoclonal)	Sigma-Aldrich	Clone 6-11B-1 Cat#MABT868	IF(1:1000)
antibody	Anti-Digoxigenin-AP (Sheep Polyclonal)	Sigma-Aldrich	Cat#11093274910	IF(1:2000)
antibody	Anti-GFP (Chicken Polyclonal)	Merck Millipore	Cat#06-896	IF(1:750)

antibody	Anti-RFP (Rabbit Polyclonal)	MBL	Cat#PM005	IF(1:750)
antibody	Myc-Tag (Mouse Monoclonal)	Cell Signaling	Clone 9B11 Cat#2276S	IF(1:1000)
antibody	Anti-GFP (Chicken Polyclonal)	Thermo Fisher	Cat#A10262	IF(1:750)
recombinant DNA reagent	PCNA-GFP	Addgene	Cat#105942	(Leung et al., 2012)
sequence-based reagent	UAS:NICD F UAS:NICD R	This paper	Genotyping primer	CATCGCGTCTCAGCCTCAC CGGAATCGTTTATTGGTGTCG 500bp band
sequence-based reagent	UAS:dnSu(H) F UAS:dnSu(H) R	This paper	Genotyping primer	GCGGTGTGTGTACTTCAGTC TCTCCCCAAACTTCCCTGTC 409bp band
sequence-based reagent	hs:dnSu(H) F hs:dnSu(H) R	This paper	Genotyping primer	CGGGCATTTACTTTATGTTGC TGCATTTCTTGCTCACTGTTTC 1kb band
commercial assay or kit	RNAscope Multiplex Fluorescent kit	Bio-techne	Cat#320850	
commercial assay or kit	mMESSAGE mMACHINE™ SP6 Transcription Kit	Thermo Fisher	Cat#AM1340	

chemical compound, drug	In-Fusion HD Cloning Plus	Takara	Cat#638910	
chemical compound, drug	ProLong Gold Antifade Mountant	Thermo Fisher	Cat#P10144	
chemical compound, drug	Hydroxyurea	Sigma-Aldrich	Cat#H8627	20μM
chemical compound, drug	Aphidicolin	Sigma-Aldrich	Cat#A0781	300μM
chemical compound, drug	Genistein	Calbiochem	Cat#345834	100μM
chemical compound, drug	Teniposide	Sigma-Aldrich	Cat#SML0609	No effect on cell cycle in zebrafish
chemical compound, drug	DAPT	Sigma-Aldrich	Cat#D5942-25MG	100μM
chemical compound, drug	Compound E	Abcam	Cat#ab142164	50μM
software, algorithm	Tamoxifen	Sigma-Aldrich	Cat#H7904	2.5μM
software, algorithm	GraphPad Prism 9	GraphPad Software		
software, algorithm	Fiji	ImageJ	(Schindelin et al., 2012)	

599 **Resource availability**
600 Further information and requests for resources and reagents should be
601 directed to and will be fulfilled by the lead contact, Claudia Linker
602 claudia.linker@kcl.ac.uk
603
604 **Materials availability**
605 Newly generated materials from this study are available by request from
606 the Lead Contact, Claudia Linker claudia.linker@kcl.ac.uk, except for
607 computational tools to be requested from Katie Bentley
608 katie.bentley@crick.ac.uk
609
610 **Data and code availability**
611 The model code is accessible at https://github.com/Bentley-Cellular-
612 Adaptive-Behaviour-Lab/NeuralCrestCpp. The code used to perform the LDA
613 analysis is accessible in the supplementary files. All numerical data used in the
614 figures is accessible in the supplementary data source file.
615 .
616
617 **Zebrafish lines and injections**
618 Zebrafish were maintained in accordance with UK Home Office regulations
619 UK Animals (Scientific Procedures) Act 1986, amended in 2013 under project
620 license P70880F4C. Embryos were obtained from the following strains: *wild type,*
621 *AB strain; Sox10:mG, Tg(-4.9sox10: Hsa.HIST1H2BJ-mCherry-2A-GLYPI-EGFP)*
622 *; Sox10:Fucci, Tg(-4.9sox10 :mAGFP-gmnn-2A-mCherry-cdt1); hs:dnSu(H),*
623 *vu21Tg (hsp70l:XdnSu(H)-myc); hs:Gal4, kca4Tg Tg(hsp70l:Gal4)1.5kca4 (1);*
624 *UAS:NICD, Tg(UAS:myc-Notch1a-intra)kca3; Sox10:Kalt4, Tg(-4.9sox10:*
625 *Hsa.HIST1H2BJ-mCherry-2A-Kalt4ER); UAS:dnSu(H), Tg(UAS:dnSu(H)-myc);*
626 *Tg(h2afva:GFP)kca13; 12XNRE:egfp.* Embryos were selected based on
627 anatomical/developmental good health and the expression of fluorescent
628 reporters when appropriate, split randomly between experimental groups and
629 maintained at 28.5°C in E3 medium. Genotyping was performed by PCR of single
630 embryos after imaging when required (UAS:NICD; UAS:dnSu(H); hs:dnSu(H)).
631 Injections were carried at 1-4 cell stage with 30pg of PCNA-GFP mRNA in a
632 volume of 1nl. mRNA was synthesised from pCS2+ PCNA-GFP plasmid, kindly
633 provided by C. Norden (IGC, Portugal), linearized with NotI and transcribed with
634 the SP6 mMessage Machine Kit (Thermo Fisher Scientific, Cat#AM1340).
635
636 **Live imaging and tracking**
637 Imaging and analysis were carried as in Alhashem et al., 2021. In short,
638 embryos were mounted in 1% agarose/E3 medium plus 40 μM Tricaine.
639 Segments 6-12 were imaged in lateral views every 5' from 16hpf for 16–18hr in
640 an upright PerkinElmer Ultraview Vox system using a 40x water immersion
641 objective. 70 μm z-stacks with 2 μm z-steps were obtained. Image stacks were
642 corrected using Correct 3D Drift Fiji and single cell tracking performed with
643 View5D Fiji plugin. Tracks were displayed using the MTrackJ and Manual

Tracking Fiji plugins. Cell area measurements were done in Fiji using the freehand selection tool to draw around cell membranes in 3D stacks using the orientation that best recapitulated the cell morphology (as in Richardson et al., 2016). Cell speed measurements were calculated from 3D tracks using the following formula: ((SQRT((X1-X2)^2+(Y1-Y2)^2+(Z1-Z2)^2))/T)*60, where X, Y and Z are the physical coordinates and T is the time-step between time-lapse frames. Ventral distances were measured in a straight line from dorsal edge of the embryo to the cell position at the end of the movie. Cell directionality measurements were calculated using a previously published Excel macro (Gorelik and Gautreau, 2014). Total duration of the cell cycle was measured between two mitotic events. Cell cycle phases duration were measured using the characteristic nuclear pattern of PCNA-GFP, in movies where only TNC (expressing RFP and GFP) were shown using this custom Fiji macro:

```
macro "Segment Nuclei [s]" {
title = getTitle();
run("Split Channels");
selectWindow("C1-" + title); //select window
with C1 in its name, nuclei should be C1
getDimensions(width, height, channelCount,
slices, frames);
run("Subtract Background...", "rolling=200
sliding stack");
setAutoThreshold("Default dark");
run("Threshold...");
setThreshold(5, 255); //change as
appropriate for your cells
setOption("BlackBackground", false);
run("Convert to Mask", "method=Default
background=Dark");
run("Close");
run("Fill Holes", "stack");
run("Despeckle", "stack");
run("Dilate", "stack");
run("Dilate", "stack");
//now go over every frame and slice
for(frame=1; frame<=frames; frame++){
for(slice=1; slice<=slices; slice++){
   selectWindow("C1-" + title);
   setSlice(slice);
   Stack.setFrame(frame);
   run("Create Selection");
   selectWindow("C2-" + title);
   setSlice(slice);
   Stack.setFrame(frame);
   run("Restore Selection");
   setBackgroundColor(0, 0, 0);
   run("Clear Outside", "slice");
```

***In situ* hybridization, immunostaining, and sectioning**

The whole mount in situ hybridization protocol was adapted from https://wiki.zfin.org/display/prot/Whole-Mount+In+Situ+Hybridization. In short, embryos were fixed overnight (O/N) in 4% Paraformaldehyde (PFA), dehydrated in 100% methanol then rehydrated, digested with proteinase K for different times depending on the stage and pre-hybridised for 2h at 65°C. Riboprobes were added, and embryos incubated at 65°C O/N. Probes were removed and embryos washed and equilibrated to PBS. Embryos were incubated in blocking solution for 2h and in anti-dig antibody O/N (Sigma-Aldrich Cat#11093274910), washed 5x30’ and NBT/BCIP colour reaction performed. Riboprobes for *notch1a, dlb (deltaB), dld (deltaD), her4, cb1045* were kindly provided by J. Lewis (CRUK); *crestin, mbp, bdh, myoD*, by S. Wilson (UCL, UK). After the in-situ colour development embryos were processed for sections, washed 5x10’ with PBS, embedded in OCT, frozen by dipping the blocks in dry ice cold 70% ETOH, and sectioned to 12-15µm using a cryostat. Sections were thawed at RT, incubated with blocking solution for 30’ (10% goat serum, 2% BSA, 0.5% Triton,

689 10mM sodium azide in PBS) and in anti-GFP antibody ON at 4°C (Merck Millipore,
690 Cat#06-896). Sections were washed with PBST 5x5' (0.5% Triton- PBS) and
691 incubated with secondary antibody for 2h at RT, mounted in ProLong™ Gold
692 Antifade Mountant (Molecular Probes Cat#P10144) and imaged. Wholemount
693 antibody staining was performed in embryos fixed for 2h in 4% PFA, washed
694 4x10', incubated in blocking solution for 2h and in primary antibodies O/N 4°C
695 (anti-myc, Cell Signaling Cat#2276S; F59 and Znp1, Developmental Studies
696 Hybridoma Bank; Acetylated tubulin, Sigma-Aldrich Cat#MABT868). Embryos
697 were washed 5x30', incubated in secondary antibodies O/N 4°C, washed 6x30'
698 and mounted in 1% agarose for imaging.
699 Imaging of sectioned and wholemount antibody-stained samples was performed
700 in PerkinElmer Ultraview Vox system.
701 RNAScope (RNAscope Fluorescent Multiplex Reagent Kit Cat#320850)
702 experiments were performed as in (Alhashem et al., 2022). In short, embryos
703 were fixed with 4% PFA overnight at 4°C and dehydrated in 100% methanol and
704 stored at -20°C until processing. All methanol was removed, and embryos were
705 air dried at room temperature for 30', permeabilised with Proteinase Plus for 10'
706 at RT (provided in kit), washed with PBS-Tween 0.01% and incubated with
707 probes for *egfp* and *sox10* or *phox2bb* at 1:100 dilution at 60°C overnight.
708 Probes were recovered, embryos washed three time with SSCT 0.2X for 15'. We
709 followed manufacturer instructions for amplification steps AMP 1-3 and HRP C1-
710 C4. Opal dyes 520, 570 and 650 (Akoya Biosciences Cat#FP1487001KT,
711 Cat#FP1488001KT and Cat#FP1496001KT) were added at 1:3000 dilution
712 followed by HRP blocker. Washes in between steps were performed with SSCT
713 0.2X for 10' twice. Primary a-GFP-Chicken (1:750) and a-RFP-Rabbit (1:750;
714 TFS Cat#A10262 and MBL Cat#PM005) antibodies diluted in blocking solution
715 (PBS-Tween 0.1%, Goat serum 5%, DMSO 1%) were added and incubated
716 overnight at 4°C. Samples were washed three times in PBS-Tween 0.1% for 1
717 hour and then incubated in secondary antibodies, a-Chicken-AlexaFluor488 and
718 a-Rabbit-AlexaFluor546 (TFS Cat#A11039 and Cat#A11010) both in a 1:1000
719 dilution in blocking solution, for 3 hours at room temperature. Samples were
720 washed six times with PBS-Tween 0.1% for 30'. For counterstaining DAPI was
721 added (1:1000) in the third wash, (Roche, Cat#10236276001, 2 mg/ml).
722 Embryos were cleared in 50% glycerol/PBS an mounted in glass bottom petri
723 dishes and imaged using Zeiss Laser Scanner Confocal Microscope 880 (405,
724 488, 514, 561 and 633 lasers).
725
726 **Drug treatments and gene expression induction**
727 Embryos were treated by adding cell cycle inhibitors to the media from 11hpf
728 and incubated for 3-12h at 28.5°C. 20μM Hydroxyurea (Sigma-Aldrich
729 Cat#H8627), 300μM Aphidicolin (Sigma-Aldrich Cat#A0781), 100μM Genistein
730 (Calbiochem Cat#345834), Teniposide (Sigma-Aldrich Cat#SML0609) or 1%
731 DMSO as control (Sigma-Aldrich Cat#D8418). Notch signalling was inhibited at
732 11hpf by adding 100μM DAPT (Sigma-Aldrich Cat#D5942-25MG) or 50μM of
733 Compound E (Abcam Cat#ab142164). The latter reagent was used to perform

734 live imaging, which is difficult to do with DAPT as it generates an interfering
735 precipitate. 1% DMSO was added as control. Gene expression was induced by
736 addition of 2.5μM of Tamoxifen (Sigma-Aldrich Cat#H7904) to the media at
737 11hpf of Sox10:Kalt4 embryos, or by heat shock at 11hpf in hs:Gal4 and
738 hs:dnSu(H) embryos by changing the media to 39°C E3, followed by 1h
739 incubation at this temperature, thereafter embryos were grown at 28.5°C to the
740 desired stage.
741
742 **Generation of UAS:dnSu(H) transgenic line**
743 Using the Infusion cloning system (Takara) the following construct was inserted
744 into the Ac/Ds vector (Chong-Morrison et al., 2018): 5xUAS sequence (Tol2Kit,
745 http://tol2kit.genetics.utah.edu/index.php/Main_Page) flanked at the 3' and 5'
746 ends by rabbit β-globin intron sequence. At the 3' end GFP followed by
747 SV40polyA sequence was cloned to generate the Ac/Ds dUAS:GFP vector. The
748 *cmlc2:egfp* transgenesis marker (Tol2Kit) was cloned after GFP in the
749 contralateral strand to prevent interaction between the UAS and the cmnl
750 sequences. The *Xenopus* dnSu(H)-myc sequence (Latimer et al., 2005) was
751 cloned into the Ac/Ds dUAS:GFP vector at the 5' end of the 5xUAS sequence,
752 followed by the SV40polyA sequence (Figure 4-figure supplement 2).
753 Transgenesis was obtained by injecting Sox10:Kalt4 embryos with 1nl containing
754 50pg of DNA plus 30pg of Ac transposase mRNA at 1 cell stage. Embryos
755 carrying the transgene were selected by heart GFP expression at 24hpf. Upon
756 Gal4ER activation by tamoxifen dnSu(H)-myc protein was readily detected with
757 anti-Myc antibody (Figure 4-figure supplement 2). GFP fluorescence driven by
758 UAS was never observed.
759
760 **Statistical analysis**
761 All graphs and statistical analysis were carried out in GraphPad Prism 9. All
762 numbers in the texts are mean ± standard deviation. Every sample was tested
763 for normality using the d'Agostino & Pearson, followed by the Shapiro-Wilk tests.
764 Samples that passed both tests were compared using either unpaired two-tailed
765 *t*-test or one-way ANOVA. Those without a normal distribution were compared
766 through a Mann-Whitney U test, Kruskal-Wallis test or Brown-Forsythe & Welch
767 ANOVA tests. For all analyses, *p* values under 0.05 were deemed statistically
768 significant, with ****$p<0.0001$, ***$p<0.001$, **$p<0.01$, and *$p<0.05$. Full
769 statistical analysis of data in Figure 5 is presented in Supplementary File 1.
770
771 **Computational model**
772 The computational model used in this study is described in Appendix 1.
773 Standard LDA analysis was carried out using the sklearn package in Python (See
774 supplementary code files).
775
776 **FIGURE LEGENDS:**
777 **Figure 1. TNC present different levels of Notch activity.**
778 A and E. Image of two different embryos Notch reporter 12xNRE:egfp (18hpf)

779 stained for *sox10* (magenta) and GFP (green) RNAs, and nuclei stained with
780 DAPI (blue).
781 B. Enlargement of the anterior area in A.
782 C. Enlargement of the more posterior area in A.
783 D. Enlargement of the anterior most posterior area in A.
784 F. Enlargement of the outlined area in E.
785 Anterior to the left, dorsal top. White lines show approximate cell boundaries.
786
787 **Figure 2. TNC induction is independent of Notch signalling after 12hpf.**
788 A. *crestin* in situ hybridisation in wildtype (WT) embryo at 18hpf.
789 B-C. *crestin* in situ hybridisation in DAPT treated embryos: (B) reduced or (C)
790 absent TNC.
791 D. Quantification of the *crestin* expression phenotypes upon DAPT treatment
792 (phenotypes: WT, black; reduced, orange; absent, red; 30% epiboly n=38, 75%
793 epiboly n=32, 11hpf n=35, 12hpf n=39).
794 E-J. In situ hybridisation for NC markers in representative control (DMSO) and
795 DAPT treated embryos from 12-16hpf. (E and F) *crestin* (DMSO n=32, DAPT
796 n=38), (G and H) *foxd3* (DMSO n=16, DAPT n=35) and (I and J) *sox10* (DMSO
797 n=27, DAPT n=29). Anterior to the left, dorsal top.
798
799 **Figure 3. Notch signalling is required for TNC migration and derivatives**
800 **formation.**
801 A-B. *Glial marker mbp* in situ hybridisation upon (A) control (DMSO; n=15) and
802 (B) DAPT (n=20) treatment from 12hpf.
803 C-D. *Neuronal marker bdh* in situ hybridisation upon (C) control (DMSO; n=25)
804 and (D) DAPT (n=18) treatment from 12hpf.
805 E-F. Pigmentation upon (E) control (DMSO; n=40) and (F) DAPT (n=52)
806 treatment from 12hpf.
807 G-H Neural crest marker *crestin* in situ hybridisation upon (G) control (DMSO)
808 and (H) DAPT treatment from 12-18hpf.
809 I-J. *crestin* in situ hybridisation upon (I) control (DMSO) and (J) DAPT treatment
810 from 12-24hpf.
811 K. Quantification of migratory chain formation upon control (DMSO) and DAPT
812 treatment from 12hpf to 18hpf (DMSO n=98; DAPT n=126), 20hpf (DMSO
813 n=111; DAPT n=109) and 24hpf (DMSO n=42; DAPT n=61).
814 L. Quantification of migratory chain formation in control (HS:Gal4; n=516),
815 Notch LOF (HS:dnSu(H); n=220) and GOF conditions (HS:Gal4xUAS:NICD;
816 n=142) heat shocked at 11hpf and analysed at 18hpf. Mann-Whitney U test,
817 control vs LOF $p<0.0001$ ****, control vs GOF $p=0.0020$ **.
818 Anterior to the left, dorsal top, except in C-D anterior left, ventral view.
819 Arrowheads indicate gene expression. All treatments performed from 12hpf.
820
821 **Figure 4. Notch activity allocates TNC migratory identity.**
822 A. Selected frames from in vivo imaging of Sox10:Kalt4 control (DMSO treated)
823 embryos.

824 B. Selected frames from control simulation with 1:3 leader/follower ratio.
825 C. Selected frames from in vivo imaging under Notch inhibited condition,
826 Sox10:Kalt4 embryos treated with CompE.
827 D. Selected frames from in vivo imaging of Notch LOF condition, Sox10:Kalt4;
828 UAS:dnSu(H) embryos.
829 E. Selected frames from all followers simulation.
830 F. Selected frames from in vivo imaging of Notch GOF condition Sox10:Kalt4;
831 UAS:NICD embryos.
832 G. Selected frames from all leaders simulation.
833 Magenta tracks and green arrowheads indicate leaders; green arrows and cyan
834 tracks follower cells. Asterisks indicate cells crossing somite borders. White line
835 marks dorsal midline. Anterior to the left, dorsal up. Time in minutes.
836
837 **Figure 5. TNC migration measurements in vivo and in-silico.**
838 A. Final position of each cell in model simulations and in vivo experiments under
839 different conditions. In-silico results depicted in confined pathway, in vivo data
840 graphed in model embryo, somites contour and dorsal midline dark grey lines,
841 edge of the premigratory area dashed lines, and NT/not boundary light grey
842 lines. Anterior left, dorsal up.
843 B. Quantification of leader overtaking events in vivo and in-silico. Leader
844 overtaken by a single follower is overtaken = 1; leader overtaken by more than
845 one follower cell is overtaken > 1.
846 C. Quantification of the ventral advance of cells in vivo and in-silico.
847 D. Quantification of cell speed in vivo and in-silico.
848 E. Quantification of cell directionality in vivo and in-silico.
849 Leader cells in magenta, followers in cyan. Magenta and cyan dashed lines
850 indicate the average values for leaders and followers respectively. Full statistical
851 analysis in Supplementary File 1.
852
853 **Figure 6. Notch signalling controls *phox2bb* expression defining leader**
854 **cells.**
855 A-B. Images of *phox2bb* expression in control embryos (Sox10:Kalt4).
856 C-D. Images of *phox2bb* expression under Notch GOF conditions (Sox10:Kalt4;
857 UAS:NICD embryos).
858 E-F. Images of *phox2bb* expression in Notch inhibition conditions (Compound E).
859 G. Quantification of *phox2bb* expression in control (n=13), Notch GOF (n=14)
860 and Notch inhibition conditions (n=11). Welch's t test, Kalt4 control vs GOF
861 $p<0.0001$ ****, DMSO control vs inhibition $p<0.0001$ ****.
862
863 **Figure 7. In-silico modelling of TNC migration.**
864 A. Schematics of model parameters. Diff CIL: only leader/follower collisions
865 induce repulsion and change of directionality. Intensity CIL: the leader's
866 response upon collision is stronger than the follower's response. Co-A: co-
867 attraction pulls together cells at a distance. Cell size: volume exclusion.
868 B. Schematics of simulations multi-objective scores.

869 C. Depiction of parameter space analysis showing the number of parameters
870 sets that fulfilled each score when different variables were tested. One leader
871 refers to chains with a single leader cell. 1:1, 1:2 and 1:3 refer to
872 leader/follower ratios.
873 D. 3D plot of LDA analysis.
874 E. LDA coefficients of in vivo data. A random dataset was used as control.
875 F. LDA Coefficients of in-silico data. A random dataset was used as control.
876
877 **Figure 8. Leaders arise from the asymmetric division of a progenitor cell**
878 **and present characteristic division patterns.**
879 A. Selected frames from in vivo imaging of leaders' progenitor division in
880 FoxD3:mCherry;H2AFVA:H2a-GFP embryos.
881 B. Area of leaders' progenitor daughter cells (n=9 cells, 7 embryos; Mann-
882 Whitney U test, p=0.0056).
883 C. Selected frames from in vivo imaging of followers' progenitor division in
884 FoxD3:mCherry;H2AFVA:H2a-GFP embryos.
885 D. Area of followers' progenitor daughter cells (n=10, 4 embryos; Mann-Whitney
886 U test, p>0.9999).
887 E. Position of progenitors' divisions on model embryo (leaders n=9, 7 embryos;
888 followers n=10, 4 embryos). PM: premigratory area; NT/not: neural
889 tube/notochord boundary.
890 F. Selected frames showing the D>M division pattern from 16-28hpf in vivo
891 imaging of a Sox10:mG embryo. Blue before-, yellow and red after-division.
892 Arrow indicates division position.
893 G. Selected frames showing the M>D division pattern from 16-28hpf in vivo
894 imaging of a Sox10:mG embryo. Labelling as in F.
895 H. Quantification of leaders' (n=21, 7 embryos) and follower's division patterns
896 (n=43, 7 embryos). Red: M>D, black: D>M.
897 I. Quantification of division positions (n=13 leaders, n=19 followers, 7 embryos;
898 Mann-Whitney U test, p=0.0002).
899 Time in minutes. Leaders in magenta, followers in cyan. Anterior left, dorsal
900 top.
901
902 **Figure 9: Cell cycle progression is required for TNC migration.**
903 A, C and E. *crestin* in situ hybridisation upon (A) DMSO, (C) Genistein or (E)
904 Aphidicolin treatment from 12-24hpf.
905 B, D and F. Enlargement of areas indicated by boxes in (A, C, E). Dotted line
906 marks NT/not boundary, arrowheads migratory chains and vertical line the chain
907 length.
908 G-H. Frequency distribution of migratory chains upon control (DMSO; n=66), (G)
909 Genistein (12h pulse, n=56; 6h pulse, n=67) or (H) Aphidicolin (12h, n=64; 3h,
910 n=79).
911 I. Cell cycle phase at migration initiation for leaders (n=38, 4 embryos) and
912 followers (n=43, 4 embryos).
913 J. Selected framed from in vivo imaging of Sox10:FUCCI. Time in minutes. Solid

914 line marks dorsal midline, dotted line marks the premigratory area. Magenta
915 arrowheads indicate leader and its daughters. Green arrowheads indicate
916 followers.
917
918 **Figure 10. Leader and follower cells progress through the cell cycle at**
919 **different rates.**
920 A. Selected frames from in vivo imaging of Sox10:Kalt4 embryos from 16-28hpf
921 injected with PCNA-GFP mRNA. White arrow points to cycling cell. Time in
922 minutes.
923 B. Quantification of the cell cycle total duration in leaders (n=20, 7 embryos)
924 and followers (n=19, 7 embryos; Unpaired t test, p=0.5240).
925 C. Quantification of the cell cycle phases duration in leaders (G1 n=45, S n=44,
926 G2 n=33 and M n=32, 11 embryos) and followers (G1 n=50, S n=48, G2 n=33
927 and M n=34, 11 embryos). Brown-Forsythe and Welch ANOVA tests, G1
928 p<0.0001, S p<0.0001, G2 p=0.9997, M p=0.9231.
929 D. Schematic representation of the cell cycle phases durations.
930
931 **Figure 11. Notch signalling regulates TNC cell cycle progression.**
932 A. Quantification of the cell cycle total duration under control (DMSO, numbers
933 as in Figure 6B) and Notch inhibition conditions (CompE, leaders n=17, followers
934 n=22, 8 embryos; one-way ANOVA, p=0.1939).
935 B. Quantification of the cell cycle phases duration under DMSO (numbers as in
936 as in Figure 6C) and Notch inhibition conditions (CompE, leaders G1 n=29, S
937 n=28, G2 n=25 and M n=25, 7 embryos; followers G1 n=32, S n=32, G2 n=30
938 and M n=30, 7 embryos; Brown-Forsythe and Welch ANOVA tests, all phases
939 G1, S, G2 and M p>0.9999 between leaders and followers.
940 C. Quantification of cell area ratio (leaders/followers) under DMSO and Notch
941 inhibited conditions (n as in D; Brown-Forsythe and Welch ANOVA tests, DMSO
942 control vs CompE All p=0.0157).
943 D. Quantification of cell area under DMSO (leaders n=26, followers n=22, 6
944 embryos) and CompE conditions (leaders n=44, followers n=41, 7 embryos).
945 Brown-Forsythe and Welch ANOVA tests, DMSO leaders vs followers p<0.0001,
946 CompE All leaders vs followers p>0.9999.
947 E-F. Frequency distribution of G1- and S-phases durations in control conditions
948 (DMSO; leaders: G1 n=45, S n=44, 11 embryos; followers: G1 n=50, S n=48,
949 11 embryos).
950 G-H. Frequency distribution of G1- and S-phases durations in Notch inhibition
951 conditions (CompE; leaders: G1 n=29, S n=28 7 embryos; followers: G1 n=32,
952 S n=32, 7 embryos).
953 I-N. Images of *phox2bb* expression in 24hpf Sox10:GFP embryo. (K-N)
954 Enlargements of follower 3 and leader cells in (I and J). Orange dotted lines
955 mark leader and third follower cell outline; white dotted lines mark follower's
956 outline.
957
958 **Figure 12. Working model of TNC migratory identity allocation through**

959 **Notch-Cell cycle interaction.**
960 A. Leader TNC progenitors divide asymmetrically giving rise to a prospective
961 leader cell that is larger than the prospective followers that arise from symmetric
962 divisions.
963 B. Interactions between TNC through Notch lateral inhibition establish higher
964 levels of Notch activity in the bigger cell, triggering the initiation of S-phase and
965 increased levels of *phox2bb* expression.
966 C. Leader cell initiated the chain movement while in S-phase trailed by followers
967 in G_1.
968 D. Loss of the leader contact with premigratory TNC allows for a new round of
969 Notch interaction that establishes a second leader cell.
970
971 **SUPPLEMENTARY FIGURES:**
972 **Figure 1-figure supplement 1. Expression of Notch signalling**
973 **components during TNC migration.**
974 Transversal sections at trunk level of Sox10:GFP embryos showing the
975 expression of:
976 A-C. *notch1a*
977 D-F. *dlb (deltaB)*
978 G-I. *dld (deltaD)*
979 J-L. *her4*
980 A, D, G and J bright field, B, E, H and K GFP-fluorescence and C, F, I and L
981 overlay. Dotted black line in the brightfield frames indicates TNC cells seen in
982 the fluorescent image.
983
984 **Figure 4-figure supplement 1. Somites and neural tissue formation are**
985 **not altered by Notch inhibition.**
986 A-B. *cb1045* in situ hybridisation upon (A) control (DMSO, n=23) and (B) DAPT
987 (n=30) treatment. Arrows indicate segmentation defects.
988 C-D. *myod* in situ hybridisation upon (C) control (DMSO, n=47) and (D) DAPT
989 (n=45) treatment.
990 E-F. *dld* (*deltaD)* in situ hybridisation upon (E) control (DMSO, n=25) and (F)
991 DAPT (n=30) treatment.
992 G-H. Antibody staining for heavy myosin (F59) upon (G) control (DMSO n=37)
993 and (H) DAPT (n=32) treatment.
994 I-J. Antibody staining for Znp1 upon (I) control (DMSO n=35) and (J) DAPT
995 (n=42) treatment.
996 K-L. Antibody staining for acetylated tubulin (Ac Tub) upon (K) control (DMSO
997 n=20) and (L) DAPT (n=27) treatment.
998 Arrowheads indicate the level at which TNC migration was analysed. Anterior to
999 the left, dorsal top.
1000
1001 **Figure 4-figure supplement 2. UAS:dnSu(H) transgenic line.**
1002 A. Diagram of the construct used to generate the UAS:dnSu(H) line.
1003 B. Scheme of protocol used.

1004 C-E. Trunk region of a Sox10:Kalt4;UAS:dnSu(H) embryo treated with tamoxifen
1005 from 11-24hpf and immunostained for (C) RFP and (D) myc. (E) overlay. Dotted
1006 squares indicate enlargement.
1007 F. Number of embryos expressing the UAS driven (myc+) after tamoxifen
1008 treatment from 11hpf for different times (15' n=20, 30' n=27, 45' n=25, 1h
1009 n=22, 3h n=18, 5h n=20, 24h n=14, 48h n=10).
1010
1011 **Figure 9-figure supplement 1. Cell cycle inhibitor drugs working**
1012 **conditions.**
1013 A. Confocal images showing nuclei and mitotic figures in Control (DMSO) and
1014 aphidicolin treated H2AFVA:H2A-GFP embryos. Arrowheads indicate mitotic figures;
1015 dashed lines mark the neural tube borders. Dorsal view, anterior to the left.
1016 B. Percentage of mitotic figures in Control (DMSO treated embryos) and
1017 embryos treated with different concentrations of cell cycle inhibitors (Kruskal-
1018 Wallis test, p<0.0001, Aphidicolin n=20 and Genistein n=32; Teniposide
1019 p>0.9999 n=27).
1020 C. Time-course of the effect of cell cycle drugs (Kruskal-Wallis test, Control vs
1021 1h Aphidicolin p=0.0007; control vs 3h, 5h and 7h Aphidicolin p<0.0001; control
1022 vs 2h, 3h and 5h Genistein p>0.0892; control vs 6h Genistein p<0.0001; control
1023 n=62 embryos; Aphidicolin 1h n=16, Aphidicolin 3h n=15, Aphidicolin 5h n=16,
1024 Aphidicolin 7h n=15; Genistein 2h n=15, Genistein 3h n=16, Genistein 5h n=17,
1025 Genistein 6h n=16).
1026 D. Quantification of cell cycle recovery times following Aphidicolin removal
1027 (control n=21; Aphidicolin 8 hours n=18, Aphidicolin 4+2h wash n=15, 4+3h
1028 wash n=15 and 4+4h wash n=15 embryos; One-way ANOVA, Control vs 8h and
1029 4+2h wash *p*<0.0001; control vs 4+3h wash and 4+4h wash *p*>0.0851).
1030 E-F. Whole mount in situ hybridisation of the NC marker *crestin* in 16hpf
1031 embryos upon (E) Aphidicolin and (F) DMSO treatment from 12hpf. Anterior to
1032 the left, dorsal top.
1033 G-H. Selected frames of in vivo imaging from Sox10:mG embryos showing cell
1034 tracks under (G) control (DMSO) 16-28hpf and (H) Aphidicolin 16-33hpf
1035 treatment. Solid line indicates the dorsal midline, dashed line the premigratory
1036 area; time in minutes.
1037 I. Quantification of the number of TNC cells per three migratory chains under
1038 control, Notch GOF and LOF conditions at either 16hpf (control n=25 embryos;
1039 GOF n=21; LOF n=14) and 22-24hpf (control n=18 embryos; GOF n=18; LOF
1040 n=9). Brown-Forsythe and Welch ANOVA tests, 16hpf: control vs GOF p>0.9999,
1041 control vs LOF p=0.9976, GOF vs LOF p=0.9942; 22-24hpf: control vs GOF
1042 p=0.8985, control vs LOF p=0.5940, GOF vs LOF p=0.3892.
1043
1044 **Figure 10-figure supplement 1. Leader and follower cells initiate**
1045 **migration at distinct cell cycle phases.**
1046 A-B. Selected frames of in vivo imaging from Sox10:Kalt4 embryos injected with
1047 PCNA-GFP mRNA, showing PCNA localization TNC. (A) Leader cell initiates
1048 migration in S-phase. (B) Follower cell divides before initiating migration in G1.

1049 Solid lines indicate embryo dorsal border, dotted lines the somite borders,
1050 segmented line the premigratory ventral border. Time in minutes. Anterior to the
1051 left, dorsal up.
1052 C. Quantification of the cell cycle phase at which cells initiate migration in PCNA-
1053 GFP mRNA injected embryos (leaders n=22, 10 embryos; followers n=45, 10
1054 embryos).
1055 D. Quantification of the cell cycle phase at which cells initiate migration in
1056 Sox10:FUCCI embryos (leaders n=38, 4 embryos; followers n=43, 4 embryos).
1057
1058 **SUPPLEMENTARY VIDEOS:**
1059 **Figure 4-video 1. Notch inhibition disrupts TNC migratory identity**
1060 **allocation.**
1061 A-B. Time lapse of Sox10:mG control (DMSO treated) embryo from 16-27hpf.
1062 C-D. Time lapse of Sox10:mG CompE treated embryo from 16-30hpf.
1063 Upper panels show fluorescent nuclei in grey and membranes in green. Lower
1064 panels show nuclei in grey, leaders tracked in magenta and followers in cyan.
1065 Arrowheads indicate leaders and arrows follower cells. Time in minutes.
1066 Related to Figures 4 and 5.
1067
1068 **Figure 4-video 2. Notch gain and loss of function disrupts TNC migratory**
1069 **identity allocation.**
1070 A-B. Time-lapse of control Sox10:Kalt4 embryo from 18-28.5hpf.
1071 C-D. Time-lapse of Notch loss of function Sox10:Kalt4;UAS:dnSu(H) embryo
1072 from 18-27.9hpf.
1073 E-F. Time-lapse of Notch gain of function, Sox10:Kalt4;UAS:NICD, embryo from
1074 18-28.5hpf.
1075 Upper panels show fluorescent nuclei in grey. Lower panels show nuclei in grey,
1076 leaders tracked in magenta and followers in cyan. Arrowheads indicate leaders,
1077 arrows follower cells. Time in minutes. Related to Figures 4 and 5.
1078
1079 **Figure 4-video 3. In-silico simulation of TNC chain migration.**
1080 A. Simulation of a population with a single leader cell (Only 1L)
1081 B. Simulation of a 1:1 leader follower ratio population (1L:1F)
1082 C. Simulation of a 1:3 leader follower ratio population (1L:3F)
1083 D. Simulation of a population composed only of follower cells (All followers)
1084 E. Simulation of a population composed only of leader cells (All leaders)
1085 Leaders tracked in magenta and followers in cyan. Arrowheads indicate leaders,
1086 arrows follower cells. Time in minutes. Related to Figures 4, 5 and 7.
1087
1088 **Figure 8-video 1. Leader cells arise from the asymmetric division of a**
1089 **progenitor cell.**

1090 3D rotation and volume reconstruction of a FoxD3:mCherry;H2aFVA:H2a-GFP
1091 specimen at 18hpf showing the daughter cells of a leader progenitor, the
1092 prospective leader in yellow, and its sibling a prospective follower in cyan.
1093 Related to Figure 8.
1094
1095 **Figure 8-video 2. Leader and follower cells present distinct division**
1096 **patterns.**
1097 M>D time-lapse of Sox10:mG embryo from 16-23hpf, showing a leader cell
1098 dividing during migration.
1099 D>M time-lapse of Sox10:mG from 16-28hpf, showing a follower cell dividing
1100 during before migration initiation.
1101 Tracks before division in blue, after division in red and yellow. Arrows indicate
1102 divisions. Imaged from 16hpf to 28hpf. Related to Figure 8.
1103
1104 **Figure 9-video 1. Cell cycle progression is required for TNC migration.**
1105 Time-lapse of control (DMSO treated) Sox10:mG embryo from 16-23hpf, and
1106 Aphidicolin treated Sox10:mG embryo from 16hpf to 30hpf.
1107 Leaders tracked in yellow, followers tracked in cyan and white. Time in minutes.
1108 Related to Figures 9 and Figure 9-figure supplement 1.
1109
1110 **Figure 9-video 2. Leader and follower cells initiate migration at different**
1111 **phases of the cell cycle.**
1112 Representative time-lapse of Sox10:FUCCI from 16-18hpf showing leaders
1113 initiate migration in S-phase, while followers emigrate in G1.
1114 Magenta arrowheads indicate the leader and its daughter cells; cyan arrowhead
1115 indicate follower cell. Time in minutes. Related to Figures 9 and Figure 9-figure
1116 supplement 1.
1117
1118 **Figure 10-video 1. PCNA-GFP reveals the cell cycle dynamics in TNC.**
1119 Time-lapse of PCNA-GFP mRNA injected Sox10:Kalt4 embryo from 20-27.6hpf.
1120 Left raw image, right the same image showing only RFP^+ TNC. Time in minutes.
1121 Related to Figures 10, 11 and Figure 9-figure supplement 1.
1122
1123 **Supplementary File 1. Statistical analysis of migratory parameters.**
1124 Related to Figure 5.

1125 **REFERENCES:**

1126 Alhashem Z, Camargo-Sosa K, Kelsh RN, Linker C. 2022. Trunk neural crest
1127 migratory position and asymmetric division predict terminal
1128 differentiation. doi:10.1101/2022.02.23.481590
1129 Alhashem Z, Portillo MA-G, Htun MR, Gauert A, Montecinos LB, Härtel S, Linker
1130 C. 2021. Zebrafish Neural Crest: Lessons and Tools to Study In vivo Cell
1131 Migration In: Campbell K, Theveneau E, editors. The Epithelial-to
1132 Mesenchymal Transition: Methods and Protocols, Methods in Molecular
1133 Biology. New York, NY: Springer US. pp. 79–106. doi:10.1007/978-1-
1134 0716-0779-4_9
1135 Ambros V. 1999. Cell cycle and cell fate in C. elegans. *Development* **126**:1947–
1136 58.
1137 Astin JW, Batson J, Kadir S, Charlet J, Persad RA, Gillatt D, Oxley JD, Nobes CD.
1138 2010. Competition amongst Eph receptors regulates contact inhibition of
1139 locomotion and invasiveness in prostate cancer cells. *Nat Cell Biol*
1140 **12**:1194–1204. doi:10.1038/ncb2122
1141 Bendris N, Lemmers B, Blanchard JM. 2015. Cell cycle, cytoskeleton dynamics
1142 and beyond: the many functions of cyclins and CDK inhibitors. *Cell Cycle*
1143 **14**:1786–1798. doi:10.1080/15384101.2014.998085
1144 Bentley K, Chakravartula S. 2017. The temporal basis of angiogenesis. *Philos*
1145 *Trans R Soc B Biol Sci* **372**:20150522. doi:10.1098/rstb.2015.0522
1146 Bentley K, Franco CA, Philippides A, Blanco R, Dierkes M, Gebala V, Stanchi F,
1147 Jones M, Aspalter IM, Cagna G, Weström S, Claesson-Welsh L, Vestweber
1148 D, Gerhardt H. 2014. The role of differential VE-cadherin dynamics in cell
1149 rearrangement during angiogenesis. *Nat Cell Biol* **16**:309–321.
1150 doi:10.1038/ncb2926
1151 Blethrow JD, Glavy JS, Morgan DO, Shokat KM. 2008. Covalent capture of
1152 kinase-specific phosphopeptides reveals Cdk1-cyclin B substrates. *Proc*
1153 *Natl Acad Sci U S A* **105**:1442–1447. doi:10.1073/pnas.0708966105
1154 Bocci F, Onuchic JN, Jolly MK. 2020. Understanding the Principles of Pattern
1155 Formation Driven by Notch Signaling by Integrating Experiments and
1156 Theoretical Models. *Front Physiol* **11**:929. doi:10.3389/fphys.2020.00929
1157 Bray SJ. 2016. Notch signalling in context. *Nat Rev Mol Cell Biol* **17**:722–735.
1158 doi:10.1038/nrm.2016.94
1159 Burstyn-Cohen T, Kalcheim C. 2002. Association between the cell cycle and
1160 neural crest delamination through specific regulation of G1/S transition.
1161 *Dev Cell* **3**:383–395.
1162 Campa VM, Gutiérrez-Lanza R, Cerignoli F, Díaz-Trelles R, Nelson B, Tsuji T,
1163 Barcova M, Jiang W, Mercola M. 2008. Notch activates cell cycle reentry
1164 and progression in quiescent cardiomyocytes. *J Cell Biol* **183**:129–141.
1165 doi:10.1083/jcb.200806104
1166 Campos AH, Wang W, Pollman MJ, Gibbons GH. 2002. Determinants of Notch-3
1167 receptor expression and signaling in vascular smooth muscle cells:
1168 implications in cell-cycle regulation. *Circ Res* **91**:999–1006.
1169 Carlson ME, Hsu M, Conboy IM. 2008. Imbalance between pSmad3 and Notch
1170 induces CDK inhibitors in old muscle stem cells. *Nature* **454**:528–532.
1171 doi:10.1038/nature07034
1172 Carrieri FA, Murray PJ, Ditsova D, Ferris MA, Davies P, Dale JK. 2019. CDK1and
1173 CDK2regulate NICD1turnover and theperiodicity of the segmentation
1174 clock. *EMBO Rep* **20**. doi:10.15252/embr.201846436

1175 Caussinus E, Colombelli J, Affolter M. 2008. Tip-Cell Migration Controls Stalk-Cell
1176 Intercalation during Drosophila Tracheal Tube Elongation. *Curr Biol*
1177 **18**:1727–1734. doi:10.1016/j.cub.2008.10.062
1178 Chen K, Jiao X, Ashton A, Di Rocco A, Pestell TG, Sun Y, Zhao J, Casimiro MC, Li
1179 Z, Lisanti MP, McCue PA, Shen D, Achilefu S, Rui H, Pestell RG. 2020. The
1180 membrane-associated form of cyclin D1 enhances cellular invasion.
1181 *Oncogenesis* **9**:83. doi:10.1038/s41389-020-00266-y
1182 Chi Y, Welcker M, Hizli AA, Posakony JJ, Aebersold R, Clurman BE. 2008.
1183 Identification of CDK2 substrates in human cell lysates. *Genome Biol*
1184 **9**:R149. doi:10.1186/gb-2008-9-10-r149
1185 Chong-Morrison V, Simoes FC, Senanayake U, Carroll DS, Riley PR, Sauka-
1186 Spengler T. 2018. Re-purposing Ac/Ds transgenic system for
1187 CRISPR/dCas9 modulation of enhancers and non-coding RNAs in
1188 zebrafish. *bioRxiv* 450684. doi:10.1101/450684
1189 Cornell RA, Eisen JS. 2005. Notch in the pathway: The roles of Notch signaling in
1190 neural crest development. *Semin Cell Dev Biol* **16**:663–672.
1191 doi:10.1016/j.semcdb.2005.06.009
1192 Cornell RA, Eisen JS. 2000. Delta signaling mediates segregation of neural crest
1193 and spinal sensory neurons from zebrafish lateral neural plate.
1194 *Development* **127**:2873–2882.
1195 Costa G, Harrington KI, Lovegrove HE, Page DJ, Chakravartula S, Bentley K,
1196 Herbert SP. 2016. Asymmetric division coordinates collective cell
1197 migration in angiogenesis. *Nat Cell Biol* **18**:1292–1301.
1198 doi:10.1038/ncb3443
1199 Creff J, Besson A. 2020. Functional Versatility of the CDK Inhibitor p57Kip2.
1200 *Front Cell Dev Biol* **8**:584590. doi:10.3389/fcell.2020.584590
1201 Dabral S, Tian X, Kojonazarov B, Savai R, Ghofrani HA, Weissmann N, Florio M,
1202 Sun J, Jonigk D, Maegel L, Grimminger F, Seeger W, Pullamsetti SS,
1203 Schermuly RT. 2016. Notch1 signalling regulates endothelial proliferation
1204 and apoptosis in pulmonary arterial hypertension. *Eur Respir J* **48**:1137–
1205 1149. doi:10.1183/13993003.00773-2015
1206 Daudet N, Żak M. 2020. Notch Signalling: The Multitask Manager of Inner Ear
1207 Development and Regeneration. *Adv Exp Med Biol* **1218**:129–157.
1208 doi:10.1007/978-3-030-34436-8_8
1209 del Álamo D, Rouault H, Schweisguth F. 2011. Mechanism and Significance of
1210 cis-Inhibition in Notch Signalling. *Curr Biol* **21**:R40–R47.
1211 doi:10.1016/j.cub.2010.10.034
1212 Devgan V, Mammucari C, Millar SE, Brisken C, Dotto GP. 2005. p21WAF1/Cip1 is
1213 a negative transcriptional regulator of Wnt4 expression downstream of
1214 Notch1 activation. *Genes Dev* **19**:1485–1495. doi:10.1101/gad.341405
1215 Fang JS, Coon BG, Gillis N, Chen Z, Qiu J, Chittenden TW, Burt JM, Schwartz MA,
1216 Hirschi KK. 2017. Shear-induced Notch-Cx37-p27 axis arrests endothelial
1217 cell cycle to enable arterial specification. *Nat Commun* **8**:2149.
1218 doi:10.1038/s41467-017-01742-7
1219 Formosa-Jordan P, Ibañes M. 2014. Competition in Notch Signaling with Cis
1220 Enriches Cell Fate Decisions. *PLoS ONE* **9**:e95744.
1221 doi:10.1371/journal.pone.0095744
1222 Gammill LS, Roffers-Agarwal J. 2010. Division of labor during trunk neural crest
1223 development. *Dev Biol* **344**:555–565. doi:10.1016/j.ydbio.2010.04.009
1224 Georgia S, Soliz R, Li M, Zhang P, Bhushan A. 2006. p57 and Hes1 coordinate
1225 cell cycle exit with self-renewal of pancreatic progenitors. *Dev Biol*
1226 **298**:22–31. doi:10.1016/j.ydbio.2006.05.036

1227 Giniger E. 1998. A Role for Abl in Notch Signaling. *Neuron* **20**:667–681.
1228 doi:10.1016/S0896-6273(00)81007-7
1229 Gorelik R, Gautreau A. 2014. Quantitative and unbiased analysis of directional
1230 persistence in cell migration. *Nat Protoc* **9**:1931–1943.
1231 doi:10.1038/nprot.2014.131
1232 Guo D, Ye J, Dai J, Li L, Chen F, Ma D, Ji C. 2009. Notch-1 regulates Akt
1233 signaling pathway and the expression of cell cycle regulatory proteins
1234 cyclin D1, CDK2 and p21 in T-ALL cell lines. *Leuk Res* **33**:678–685.
1235 doi:10.1016/j.leukres.2008.10.026
1236 Hadjivasiliou Z, Moore RE, McIntosh R, Galea GL, Clarke JDW, Alexandre P.
1237 2019. Basal Protrusions Mediate Spatiotemporal Patterns of Spinal Neuron
1238 Differentiation. *Dev Cell* **49**:907-919.e10.
1239 doi:10.1016/j.devcel.2019.05.035
1240 Hirota T, Morisaki T, Nishiyama Y, Marumoto T, Tada K, Hara T, Masuko N,
1241 Inagaki M, Hatakeyama K, Saya H. 2000. Zyxin, a regulator of actin
1242 filament assembly, targets the mitotic apparatus by interacting with h-
1243 warts/LATS1 tumor suppressor. *J Cell Biol* **149**:1073–1086.
1244 doi:10.1083/jcb.149.5.1073
1245 Hochgreb-Hägele T, Bronner ME. 2013. A novel FoxD3 gene trap line reveals
1246 neural crest precursor movement and a role for FoxD3 in their
1247 specification. *Dev Biol* **374**:1–11. doi:10.1016/j.ydbio.2012.11.035
1248 Hunter GL, Hadjivasiliou Z, Bonin H, He L, Perrimon N, Charras G, Baum B.
1249 2016. Coordinated control of Notch/Delta signalling and cell cycle
1250 progression drives lateral inhibition-mediated tissue patterning.
1251 *Development* **143**:2305–2310. doi:10.1242/dev.134213
1252 Joshi I, Minter LM, Telfer J, Demarest RM, Capobianco AJ, Aster JC, Sicinski P,
1253 Fauq A, Golde TE, Osborne BA. 2009. Notch signaling mediates G1/S cell-
1254 cycle progression in T cells via cyclin D3 and its dependent kinases. *Blood*
1255 **113**:1689–1698. doi:10.1182/blood-2008-03-147967
1256 Kagawa Y, Matsumoto S, Kamioka Y, Mimori K, Naito Y, Ishii T, Okuzaki D,
1257 Nishida N, Maeda S, Naito A, Kikuta J, Nishikawa K, Nishimura J,
1258 Haraguchi N, Takemasa I, Mizushima T, Ikeda M, Yamamoto H, Sekimoto
1259 M, Ishii H, Doki Y, Matsuda M, Kikuchi A, Mori M, Ishii M. 2013. Cell Cycle-
1260 Dependent Rho GTPase Activity Dynamically Regulates Cancer Cell Motility
1261 and Invasion In vivo. *PLOS ONE* **8**:e83629.
1262 doi:10.1371/journal.pone.0083629
1263 Kohrman AQ, Matus DQ. 2017. Divide or Conquer: Cell Cycle Regulation of
1264 Invasive Behavior. *Trends Cell Biol* **27**:12–25.
1265 doi:10.1016/j.tcb.2016.08.003
1266 Konen J, Summerbell E, Dwivedi B, Galior K, Hou Y, Rusnak L, Chen A, Saltz J,
1267 Zhou W, Boise LH, Vertino P, Cooper L, Salaita K, Kowalski J, Marcus AI.
1268 2017. Image-guided genomics of phenotypically heterogeneous
1269 populations reveals vascular signalling during symbiotic collective cancer
1270 invasion. *Nat Commun* **8**:15078. doi:10.1038/ncomms15078
1271 Koon YL, Zhang S, Rahmat MB, Koh CG, Chiam K-H. 2018. Enhanced Delta-
1272 Notch Lateral Inhibition Model Incorporating Intracellular Notch
1273 Heterogeneity and Tension-Dependent Rate of Delta-Notch Binding that
1274 Reproduces Sprouting Angiogenesis Patterns. *Sci Rep* **8**:9519.
1275 doi:10.1038/s41598-018-27645-1
1276 Kur E, Kim J, Tata A, Comin CH, Harrington KI, Costa L da F, Bentley K, Gu C.
1277 2016. Temporal modulation of collective cell behavior controls vascular
1278 network topology. *eLife* **5**:e13212. doi:10.7554/eLife.13212

1279 Latimer AJ, Shin J, Appel B. 2005. her9 promotes floor plate development in
1280 zebrafish. *Dev Dyn* **232**:1098–1104.
1281 doi:https://doi.org/10.1002/dvdy.20264
1282 Leslie JD, Ariza-McNaughton L, Bermange AL, McAdow R, Johnson SL, Lewis J.
1283 2007. Endothelial signalling by the Notch ligand Delta-like 4 restricts
1284 angiogenesis. *Development* **134**:839–844. doi:10.1242/dev.003244
1285 Leung L, Klopper AV, Grill SW, Harris WA, Norden C. 2012. Apical migration of
1286 nuclei during G2 is a prerequisite for all nuclear motion in zebrafish
1287 neuroepithelia. *Development* **138**:5003–5013. doi:10.1242/dev.071522
1288 Lewis J. 1998. Notch signalling and the control of cell fate choices in vertebrates
1289 **9**:583–589.
1290 Li Z, Wang C, Prendergast GC, Pestell RG. 2006. Cyclin D1 functions in cell
1291 migration. *Cell Cycle Georget Tex* **5**:2440–2442.
1292 doi:10.4161/cc.5.21.3428
1293 Liu Z, Brunskill E, Boyle S, Chen S, Turkoz M, Guo Y, Grant R, Kopan R. 2015.
1294 Second-generation Notch1 activity-trap mouse line (N1IP::CreHI)
1295 provides a more comprehensive map of cells experiencing Notch1 activity.
1296 *Development* **142**:1193–1202. doi:10.1242/dev.119529
1297 Lukoseviciute M, Gavriouchkina D, Williams RM, Hochgreb-Hagele T, Senanayake
1298 U, Chong-Morrison V, Thongjuea S, Repapi E, Mead A, Sauka-Spengler T.
1299 From Pioneer to Repressor: Bimodal foxd3 Activity Dynamically Remodels
1300 Neural Crest Regulatory Landscape In vivo. *Dev Cell* **47**:608-628.e6.
1301 doi:10.1016/j.devcel.2018.11.009
1302 Maguire LH, Thomas AR, Goldstein AM. 2015. Tumors of the neural crest:
1303 Common themes in development and cancer. *Dev Dyn* **244**:311–322.
1304 doi:10.1002/dvdy.24226
1305 Mammucari C, Vignano AT di, Sharov AA, Neilson J, Havrda MC, Roop DR,
1306 Botchkarev VA, Crabtree GR, Dotto GP. 2005. Integration of Notch 1 and
1307 Calcineurin/NFAT Signaling Pathways in Keratinocyte Growth and
1308 Differentiation Control. *Dev Cell* **8**:665–676.
1309 doi:10.1016/j.devcel.2005.02.016
1310 Manes T, Zheng D-Q, Tognin S, Woodard AS, Marchisio PC, Languino LR. 2003.
1311 αvβ3 integrin expression up-regulates cdc2, which modulates cell
1312 migration. *J Cell Biol* **161**:817–826. doi:10.1083/jcb.200212172
1313 Molinie N, Rubtsova SN, Fokin A, Visweshwaran SP, Rocques N, Polesskaya A,
1314 Schnitzler A, Vacher S, Denisov EV, Tashireva LA, Perelmuter VM,
1315 Cherdyntseva NV, Bièche I, Gautreau AM. 2019. Cortical branched actin
1316 determines cell cycle progression. *Cell Res*. doi:10.1038/s41422-019-
1317 0160-9
1318 Moro E, Vettori A, Porazzi P, Schiavone M, Rampazzo E, Casari A, Ek O,
1319 Facchinello N, Astone M, Zancan I, Milanetto M, Tiso N, Argenton F. 2013.
1320 Generation and application of signaling pathway reporter lines in
1321 zebrafish. *Mol Genet Genomics* **288**:231–242. doi:10.1007/s00438-013-
1322 0750-z
1323 Morse PM. 1929. Diatomic Molecules According to the Wave Mechanics. II.
1324 Vibrational Levels. Phys Rev 34:57–64. doi:10.1103/PhysRev.34.57
1325 Nagai T, Ishikawa T, Minami Y, Nishita M. 2020. Tactics of cancer invasion:
1326 solitary and collective invasion. *J Biochem (Tokyo)* mvaa003.
1327 doi:10.1093/jb/mvaa003
1328 Nguyen B-C, Lefort K, Mandinova A, Antonini D, Devgan V, Della Gatta G, Koster
1329 MI, Zhang Z, Wang J, di Vignano AT, Kitajewski J, Chiorino G, Roop DR,
1330 Missero C, Dotto GP. 2006. Cross-regulation between Notch and p63 in

1331 keratinocyte commitment to differentiation. *Genes Dev* **20**:1028–1042.
1332 doi:10.1101/gad.1406006
1333 Nicoli S, Knyphausen C-P, Zhu LJ, Lakshmanan A, Lawson ND. 2012. miR-221 is
1334 required for endothelial tip cell behaviors during vascular development.
1335 *Dev Cell* **22**:418–429. doi:10.1016/j.devcel.2012.01.008
1336 Noseda M, Chang L, McLean G, Grim JE, Clurman BE, Smith LL, Karsan A. 2004.
1337 Notch activation induces endothelial cell cycle arrest and participates in
1338 contact inhibition: role of p21Cip1 repression. *Mol Cell Biol* **24**:8813–
1339 8822. doi:10.1128/MCB.24.20.8813-8822.2004
1340 Nusser-Stein S, Beyer A, Rimann I, Adamczyk M, Piterman N, Hajnal A, Fisher J.
1341 2012. Cell-cycle regulation of NOTCH signaling during C. elegans vulval
1342 development. *Mol Syst Biol* **8**. doi:10.1038/msb.2012.51
1343 Ohnuma S, Philpott A, Wang K, Holt CE, Harris WA. 1999. p27Xic1, a Cdk
1344 Inhibitor, Promotes the Determination of Glial Cells in Xenopus Retina.
1345 *Cell* **99**:499–510. doi:10.1016/S0092-8674(00)81538-X
1346 Palomero T, Lim WK, Odom DT, Sulis ML, Real PJ, Margolin A, Barnes KC, O'Neil
1347 J, Neuberg D, Weng AP, Aster JC, Sigaux F, Soulier J, Look AT, Young RA,
1348 Califano A, Ferrando AA. 2006. NOTCH1 directly regulates c-MYC and
1349 activates a feed-forward-loop transcriptional network promoting leukemic
1350 cell growth. *Proc Natl Acad Sci* **103**:18261–18266.
1351 doi:10.1073/pnas.0606108103
1352 Pandya P, Orgaz JL, Sanz-Moreno V. 2017. Actomyosin contractility and
1353 collective migration: may the force be with you. *Curr Opin Cell Biol*
1354 **48**:87–96. doi:10.1016/j.ceb.2017.06.006
1355 Park H-C, Boyce J, Shin J, Appel B. 2005. Oligodendrocyte specification in
1356 zebrafish requires notch-regulated cyclin-dependent kinase inhibitor
1357 function. *J Neurosci Off J Soc Neurosci* **25**:6836–6844.
1358 doi:10.1523/JNEUROSCI.0981-05.2005
1359 Parkinson E, Edwards J. 1978. Non-reciprocal contact inhibition of locomotion of
1360 chick embryonic choroid fibroblasts by pigmented retina epithelial cells. *J*
1361 *Cell Sci* **33**:103–120.
1362 Patel J, Wong HY, Wang W, Alexis J, Shafiee A, Stevenson AJ, Gabrielli B, Fisk
1363 NM, Khosrotehrani K. 2016. Self-Renewal and High Proliferative Colony
1364 Forming Capacity of Late-Outgrowth Endothelial Progenitors Is Regulated
1365 by Cyclin-Dependent Kinase Inhibitors Driven by Notch Signaling. *Stem*
1366 *Cells Dayt Ohio* **34**:902–912. doi:10.1002/stem.2262
1367 Pauls S, Geldmacher-Voss B, Campos-Ortega JA. 2001. A zebrafish histone
1368 variant H2A.F/Z and a transgenic H2A.F/Z:GFP fusion protein for in vivo
1369 studies of embryonic development. *Dev Genes Evol* **211**:603–610.
1370 doi:10.1007/s00427-001-0196-x
1371 Phng L-K, Gerhardt H. 2009. Angiogenesis: A Team Effort Coordinated by Notch.
1372 *Dev Cell* **16**:196–208. doi:10.1016/j.devcel.2009.01.015
1373 Rajan SG, Gallik KL, Monaghan JR, Uribe RA, Bronner ME, Saxena A. 2018.
1374 Tracking neural crest cell cycle progression in vivo. *genesis* **56**:e23214.
1375 doi:10.1002/dvg.23214
1376 Rangarajan A, Talora C, Okuyama R, Nicolas M, Mammucari C, Oh H, Aster JC,
1377 Krishna S, Metzger D, Chambon P, Miele L, Aguet M, Radtke F, Dotto GP.
1378 2001. Notch signaling is a direct determinant of keratinocyte growth
1379 arrest and entry into differentiation. *EMBO J* **20**:3427–3436.
1380 doi:10.1093/emboj/20.13.3427

1381 Reichrath, J., Reichrath, S., 2012. Notch signaling in embryology and cancer,
1382 Advances in experimental medicine and biology. Springer
1383 Science+Business Media ; Landes Bioscience, New York : Austin, Tex.
1384 Riahi R, Sun J, Wang S, Long M, Zhang DD, Wong PK. 2015. Notch1–Dll4
1385 signalling and mechanical force regulate leader cell formation during
1386 collective cell migration. *Nat Commun* **6**:6556. doi:10.1038/ncomms7556
1387 Riccio O, van Gijn ME, Bezdek AC, Pellegrinet L, van Es JH, Zimber-Strobl U,
1388 Strobl LJ, Honjo T, Clevers H, Radtke F. 2008. Loss of intestinal crypt
1389 progenitor cells owing to inactivation of both Notch1 and Notch2 is
1390 accompanied by derepression of CDK inhibitors p27Kip1 and p57Kip2.
1391 *EMBO Rep* **9**:377–383. doi:10.1038/embor.2008.7
1392 Richardson J, Gauert A, Briones Montecinos L, Fanlo L, Alhashem ZM, Assar R,
1393 Marti E, Kabla A, Härtel S, Linker C. 2016. Leader Cells Define
1394 Directionality of Trunk, but Not Cranial, Neural Crest Cell Migration. *Cell*
1395 *Rep* **15**:2076–2088. doi:10.1016/j.celrep.2016.04.067
1396 Richter S, Schulze U, Tomançak P, Oates AC. 2017. Small molecule screen in
1397 embryonic zebrafish using modular variations to target segmentation. *Nat*
1398 *Commun* **8**:1901. doi:10.1038/s41467-017-01469-5
1399 Ridgway J, Zhang G, Wu Y, Stawicki S, Liang W-C, Chanthery Y, Kowalski J,
1400 Watts RJ, Callahan C, Kasman I, Singh M, Chien M, Tan C, Hongo J-AS, de
1401 Sauvage F, Plowman G, Yan M. 2006. Inhibition of Dll4 signalling inhibits
1402 tumour growth by deregulating angiogenesis. *Nature* **444**:1083–1087.
1403 doi:10.1038/nature05313
1404 Rios AC, Serralbo O, Salgado D, Marcelle C. 2011. Neural crest regulates
1405 myogenesis through the transient activation of NOTCH. *Nature* **473**:532–
1406 535. doi:10.1038/nature09970
1407 Rizzo P, Miao H, D'Souza G, Osipo C, Yun J, Zhao H, Mascarenhas J, Wyatt D,
1408 Antico G, Hao L, Yao K, Rajan P, Hicks C, Siziopikou K, Selvaggi S, Bashir
1409 A, Bhandari D, Marchese A, Lendahl U, Qin J-Z, Tonetti DA, Albain K,
1410 Nickoloff BJ, Miele L. 2008. Cross-talk between Notch and the Estrogen
1411 Receptor in Breast Cancer Suggests Novel Therapeutic Approaches.
1412 *Cancer Res* **68**:5226–5235. doi:10.1158/0008-5472.CAN-07-5744
1413 Ronchini C, Capobianco AJ. 2001. Induction of Cyclin D1 Transcription and CDK2
1414 Activity by Notchic: Implication for Cell Cycle Disruption in Transformation
1415 by Notchic. *Mol Cell Biol* **21**:5925–5934. doi:10.1128/MCB.21.17.5925-
1416 5934.2001
1417 Rørth P. 2009. Collective Cell Migration. *Annu Rev Cell Dev Biol* **25**:407–429.
1418 doi:10.1146/annurev.cellbio.042308.113231
1419 Rowan S, Conley KW, Le TT, Donner AL, Maas RL, Brown NL. 2008. Notch
1420 signaling regulates growth and differentiation in the mammalian lens. *Dev*
1421 *Biol* **321**:111–122. doi:10.1016/j.ydbio.2008.06.002
1422 Scheer N, Campos-Ortega JA. 1999. Use of the Gal4-UAS technique for targeted
1423 gene expression in the zebrafish. *Mech Dev* **80**:153–158.
1424 Schindelin J, Arganda-Carreras I, Frise E, Kaynig V, Longair M, Pietzsch T,
1425 Preibisch S, Rueden C, Saalfeld S, Schmid B, Tinevez J-Y, White DJ,
1426 Hartenstein V, Eliceiri K, Tomancak P, Cardona A. 2012. Fiji: an open-
1427 source platform for biological-image analysis. *Nat Methods* **9**:676–682.
1428 doi:10.1038/nmeth.2019
1429 Song Y, Zhao C, Dong L, Fu M, Xue L, Huang Z, Tong T, Zhou Z, Chen A, Yang
1430 Z, Lu N, Zhan Q. 2008. Overexpression of cyclin B1 in human esophageal
1431 squamous cell carcinoma cells induces tumor cell invasive growth and
1432 metastasis. *Carcinogenesis* **29**:307–315. doi:10.1093/carcin/bgm269

1433 Theveneau E, Duband J-L, Altabef M. 2007. Ets-1 Confers Cranial Features on
1434 Neural Crest Delamination. *PLoS ONE* **2**:e1142.
1435 doi:10.1371/journal.pone.0001142
1436 Theveneau E, Linker C. 2017. Leaders in collective migration: are front cells
1437 really endowed with a particular set of skills? *F1000Research* **6**.
1438 Theveneau E, Mayor R. 2013. Collective cell migration of epithelial and
1439 mesenchymal cells. *Cell Mol Life Sci* **70**:3481–3492. doi:10.1007/s00018-
1440 012-1251-7
1441 Timmerman LA. 2004. Notch promotes epithelial-mesenchymal transition during
1442 cardiac development and oncogenic transformation. *Genes Dev* **18**:99–
1443 115. doi:10.1101/gad.276304
1444 Venkatraman L, Regan ER, Bentley K. 2016. Time to Decide? Dynamical Analysis
1445 Predicts Partial Tip/Stalk Patterning States Arise during Angiogenesis.
1446 *PLOS ONE* **11**:e0166489. doi:10.1371/journal.pone.0166489
1447 Walmod PS, Hartmann-Petersen R, Prag S, Lepekhin EL, Röpke C, Berezin V,
1448 Bock E. 2004. Cell-cycle-dependent regulation of cell motility and
1449 determination of the role of Rac1. *Exp Cell Res* **295**:407–420.
1450 doi:10.1016/j.yexcr.2004.01.011
1451 Yoon M-K, Mitrea DM, Ou L, Kriwacki RW. 2012. Cell cycle regulation by the
1452 intrinsically disordered proteins p21 and p27. *Biochem Soc Trans* **40**:981–
1453 988. doi:10.1042/BST20120092
1454 Zalc A, Hayashi S, Auradé F, Bröhl D, Chang T, Mademtzoglou D, Mourikis P, Yao
1455 Z, Cao Y, Birchmeier C, Relaix F. 2014. Antagonistic regulation of p57kip2
1456 by Hes/Hey downstream of Notch signaling and muscle regulatory factors
1457 regulates skeletal muscle growth arrest. *Dev Camb Engl* **141**:2780–2790.
1458 doi:10.1242/dev.110155
1459 Zatulovskiy E, Skotheim JM. 2020. On the Molecular Mechanisms Regulating
1460 Animal Cell Size Homeostasis. *Trends Genet* **36**:360–372.
1461 doi:10.1016/j.tig.2020.01.011
1462 Zhong Z, Yeow W-S, Zou C, Wassell R, Wang C, Pestell RG, Quong JN, Quong
1463 AA. 2010. Cyclin D1/cyclin-dependent kinase 4 interacts with filamin A
1464 and affects the migration and invasion potential of breast cancer cells.
1465 *Cancer Res* **70**:2105–2114. doi:10.1158/0008-5472.CAN-08-1108
1466

Appendix 1: Computer Modelling Methods

A minimal discrete element model of TNC migration was developed in which each cell is modelled as an infinitesimal particle moving in 2D space. A network of neighbours within the particle system is identified by a Delaunay triangulation (Figure 1a).

Equation 1: $V(r) = D_e\left(e^{-2a(r-r_e)} - 2e^{-a(r-r_e)}\right),\ \ a = \sqrt{k/\ 2D_e}$

Thus defined, the system exhibits Brownian dynamics as described by the over-damped Langevin equation [Equation 2], such that the velocity of each particle is proportional to the resultant force applied to it (∇V), plus a stochastic component (ζ).

Equation 2: $\underline{\dot{x}} = -\frac{\Delta V}{\gamma} + \underline{\zeta}$

Components of the resultant force on each cell arise from cell-cell interactions, cell-boundary interactions, and cell autonomous motio

a. Tissue environment (boundary)

Cells move into permissive space between the neural tube/notochord and the somites. Boundary locations are specified before any simulation. The boundary is implemented as a region of space that applies strong repulsion to nearby cells (Figure 1e). Any cell that moves within a cell radius of the boundary experiences a force given by the gradient of the same Morse potential used in cell-cell interactions, such that the repulsion of any cell from the boundary depends upon the cell volume exclusion and increases exponentially as the cell approaches the boundary (Figure 1e).

The size and shape of the boundary represent a space for the pre-migratory cells at the top, a space in the middle where the notochord and neural tube meet (midline) and a vertical space where the chain can proceed downwards. The dimensions of the environment boundary were calibrated to *in vivo* measurements (Figure 1e – showing micron scale dimensions on the boundary).

The system is setup in a 'T' shape, which is interrupted in the middle by a space of horizontal mobility, because *in vivo* cells regularly move into this space. The wider region at the top represents the premigratory zone (PMZ) at the top of each migratory chain. Cells are able to filter in from the sides to mimic the continuous clustering of cells above migration chains.

b. Cell properties/ behaviours

b.1. Contact inhibition and autonomous motion

Cells exhibit autonomous motion in a direction determined by their internal polarisation. This polarisation is influenced by interaction with the cell's neighbours, such that the cell will try to move into empty space. We introduce contact inhibition into the model as a term in the Langevin equation [Equation 2], with magnitude determined by a user-defined parameter. The direction of autonomous magnitude for a given cell is found by identifying all adjacent nearest neighbours surrounding the cell, calculating the angle subtended by each adjacent pair, and bisecting the largest such angle (Figure 1d). The magnitude of this autonomous velocity component is proportional to the user-defined parameter (aMag) and the square of the maximum subtended angle, representing the combined effect of greater

polarisation and more free space to move into. Any cell that moves beyond a threshold distance from its nearest neighbour will stop autonomous motion, modelling the loss of polarisation when losing contact with neighbouring cells.

b.2. Cell volume exclusion

Cells exhibit volume exclusion (two cells repel from one another if they get closer than an equilibrium distance). This simply models how two cells cannot occupy the same space at the same time. The extent to which volume exclusion is exhibited can be thought of as the level of cell stiffness. Low *k* means cells are squishier. This is modelled using the *k* term in the Morse potential calculation [Equation 1].

b.3. Co-attraction (co-A)

When cells drift more than the equilibrium distance apart, they are drawn back toward their neighbours with a force calculated by the Morse potential curve [Equation 1].

c. Migratory Identity

Leader and follower migratory identities were allocated to cells according to the order in which these enter the chain. That is, the first cell becomes leader then the next X many cells become follower cells before the cell after that becomes leader. A sensitivity analysis on leader cells frequency was performed by spacing parameter S.

d. Simulation procedure

The simulation follows the process steps in Figure 2 and was simulated on CAMP – the Francis Crick Institute's Linux-based high-performance computing system. Parameter combination/ experimental condition pairs were run 100 times in parallel across 10 nodes.

e. Parameterisation

Time was calibrated as follows: *in vivo* control cells tend to migrate to approximately 120 microns from dorsal midline on average (Figure 3F main text). The total time of migration is on average 11.64h long (~700 minutes). In 2000 timesteps, the control case (with differential CIL, heterogenous migratory identities and S = "1:3") also migrates to approximately 120mm. We gathered data every 20 timesteps, which means in our simulation movies there are 100 frames (i.e., 1 frame = 7 minutes).

Where possible parameters were calibrated to values measured *in vivo* (Table 1). Model specific parameters unable to be linked directly to *in vivo* values were set to values that produced realistic bounds of behaviour.

Table 1. Simulation parameters, description, range and source

Name	Description	Range	ptimised setting	Units	Source
PMZ width	Horizontal space of the premigratory zone	57.0	57.0	μm	Measurement
PMZ height	Vertical space in the premigratory zone	28.5	28.5	μm	Measurement
CE widt	Horizontal width in the migratory chain	22.8	22.8	μm	Model specific
MZ rati	Vertical space around the midpoint relative to the height of the PMZ	0.5	0.5	Units	Model specific
Cell radius	Interaction radius of cell radius was inferred assuming cells were perfect spheres, based on volumetric measurements (Richardson et al., 2016)	7.4	7.4	mm	Measurement
Nc	Number of cells	18	18	Numbe	Measurement
ζ	Magnitude of stochastic component. Term of the Langevin equation, which controls random cell movement magnitude	0.035	0.035	Units	Model specific
γ	Overdamped Langevin equation drag factor.	1	1	Units	Model specific
S	Leader spacing- number of follower cells between leader cells in migration	{0, 1, 2, 3, ∞}	3	Numbe	Calibrated
Followe k	Spring constant near equilibrium (parameter of Morse potential) for follower type cells. This can be thought of as the cell volume exclusion of the cells. High k means that cells are stiffer.	Low: [0.01] Medium: [0.02] High: [0.03]	0.01	Units	Calibrated
Leader	As above but for leader type cells.	Low: [0.01] Medium: [0.02] High: [0.03]	0.02	Units	Calibrated
Followe De	Depth of potential well (parameter of Morse potential). Greater De means greater range of co-attraction. This can be thought of as the amount of chemotactic attraction signal release by each cell.	Low: [3e-05] Medium: [6e-05] High: [9e-05]	3e-05	Units	Calibrated
Leader De	As above but for leader type cells.	Low: [3e-05] Medium: [6e-05] High: [9e-05]	6e-05	Units	Calibrated
Followe aMag	Magnitude of autonomous cell velocity. In the model's implementation of contact inhibition,	Low: [1.1e-07	1.1e-0	Units	Calibrated

	cells move into the widest open space. This parameter modulates the velocity with which they move into this space.	Medium: [1.56e-06] High: [3e-06]			
Leader aMag	As above but for leader type cells.	Low: [1.1e-07 Medium: [1.56e-06] High: [3e-06]	3e-06	Units	Calibrated
Interaction threshold	Multiples of cell radii beyond which neighbours no longer cause polarisation by contact inhibition.	1	1	Units	Model specific
T max	Total run time in arbitrary units.	2000	2000	Units	Model specific
dt	Time interval between iterations.	0.1	0.1	Units	Model specific
Output interval	Time interval between data outputs.	10	10	Units	Model specific

f. Sensitivity analysis

In the grid search calibration approach we fixed follower cells properties to be at their low levels. Next, we looked at how changes to leader cell physical properties affected ventral distance (Figure 3). This shows a strong effect in leader aMag, whereby low leader aMag resulted in cells not migrating much beyond 100 microns no matter the level of co-attraction or cell volume exclusion. aMag had to be varied across a wider range to see a clear effect. Through this, aMag has a dominating effect on ventral distance: higher aMag is associated with higher ventral distance.

Figure legends:

Appendix 1-figure 1. Description of model mechanisms and configuration

a) Diagram of 10 cells modelled as infinitesimal particles, with Delaunay triangulation showing nearest neighbours and circles showing typical cell radii around each particle.

b) Morse potential for low volume exclusion k (orange), high cell volume exclusion (blue), high energy depth De (solid line), and low energy depth (dashed line). The portion of the curve that relates to repulsion is distinguished from the portion that relates to attraction by the vertical green line.

c) Demonstrating calculation of force component from a boundary. When the centre point of a cell moves within a cell radius of the boundary, the cell experiences a force perpendicular to and away from the boundary with magnitude determined by a Morse potential and with offset from equilibrium distance.

d) Demonstrating calculation of cell polarisation. Adjacent nearest neighbours of a cell subtend angles θ1, θ2, and θ3 around the cell centre. The direction of polarisation, and hence autonomous motion, bisects θ3, the largest such angle. Forces on each cell arise from interactions between neighbouring particles. These interactions are defined by a Morse potential [Morse, 1929], a function of the separation between particles, and parameterised by an equilibrium separation (re), approximate spring constant (k), and energy depth (De) [Equation 1, Figure 1b]. These parameters model the typical radius of a cell, its volume exclusion, and chemoattractive magnitude ("co-attraction").

e) Dimensions of the model. White space represents empty space where cells can move freely, black space is space where cells cannot move due to boundaries. Horizontal

movement is restricted while moving down the chain except for in the middle zone (for values associated with these parameters see table 1).

Appendix 1-figure 2. Model pseudocode overview.

A predefined number of cells is initialised in the PMZ. Thereafter, the system enters a loop for every time step up to tmax. In this loop, forces are linearly summed to obtain each cell's velocity vector for that time step:

1) a Delaunay triangulation is performed on cells.
2) Each cell's nearest neighbours are identified.
3) Local forces between cells are calculated according to the Morse potential (Figure 1b).
4) Boundary forces are applied to each cell.
5) Autonomous motion and contact inhibition are calculated for each cell.
6) Gaussian noise is added to each cell's velocity vector.
7) The system's clock is updated, as well as each cell's position.
8) Experimental conditions are applied for the next time step (e.g., giving certain cells leader qualities).

Appendix 1-figure 3. Calibration on final position of the furthest travelling cell in microns.

The optimal distance is 120 microns which is shown by the pink square. Ventral distance increases with increases in cell volume exclusion and co-attraction, which is most apparent in the rightmost heatmap.

Table 1. Simulation parameters, description, range and source

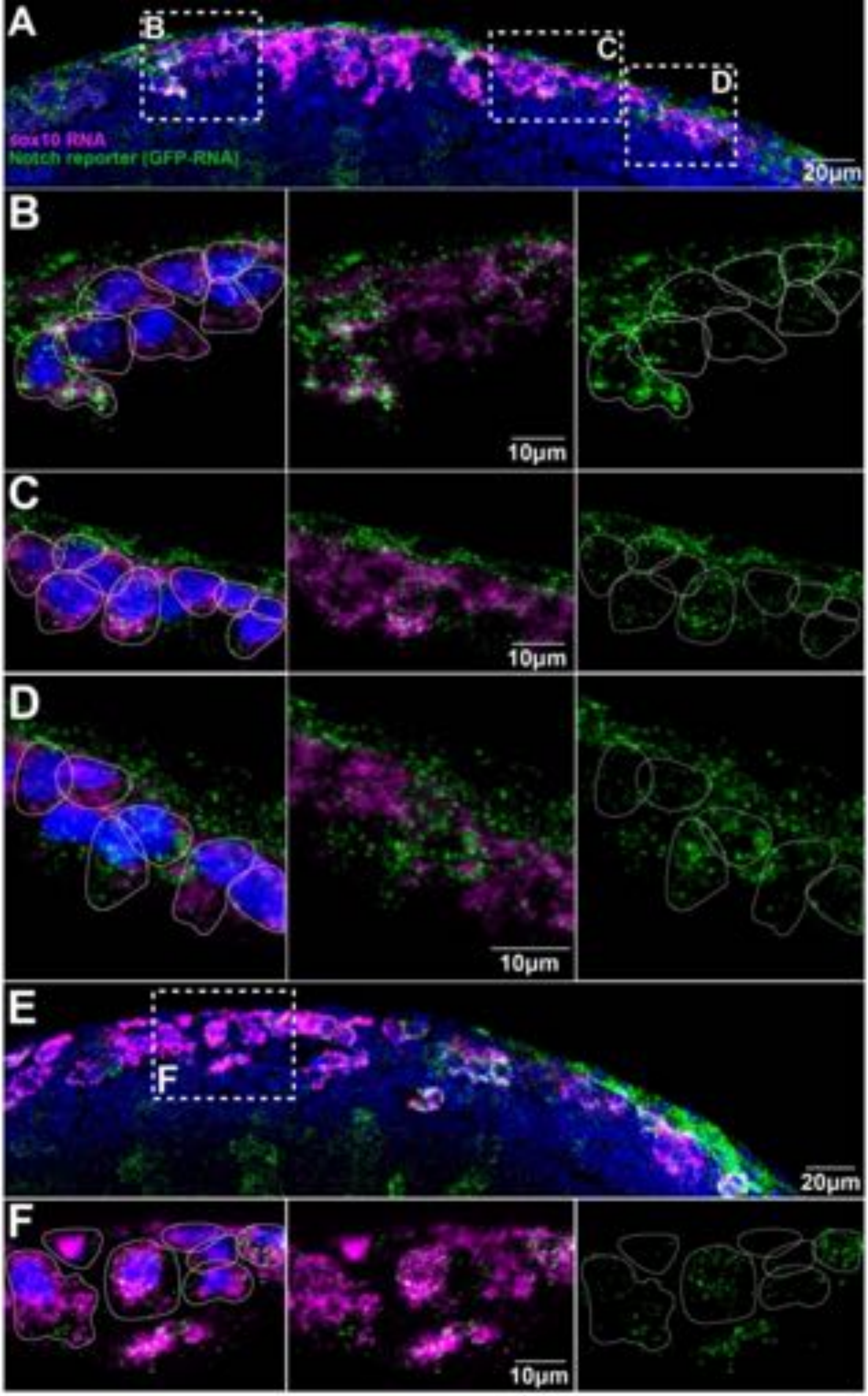
A
B
C
D
Sox10 RNA
Notch reporter (GFP-RNA)
20µm
B
10µm
C
10µm
D
10µm
E
F
20µm
F
10µm

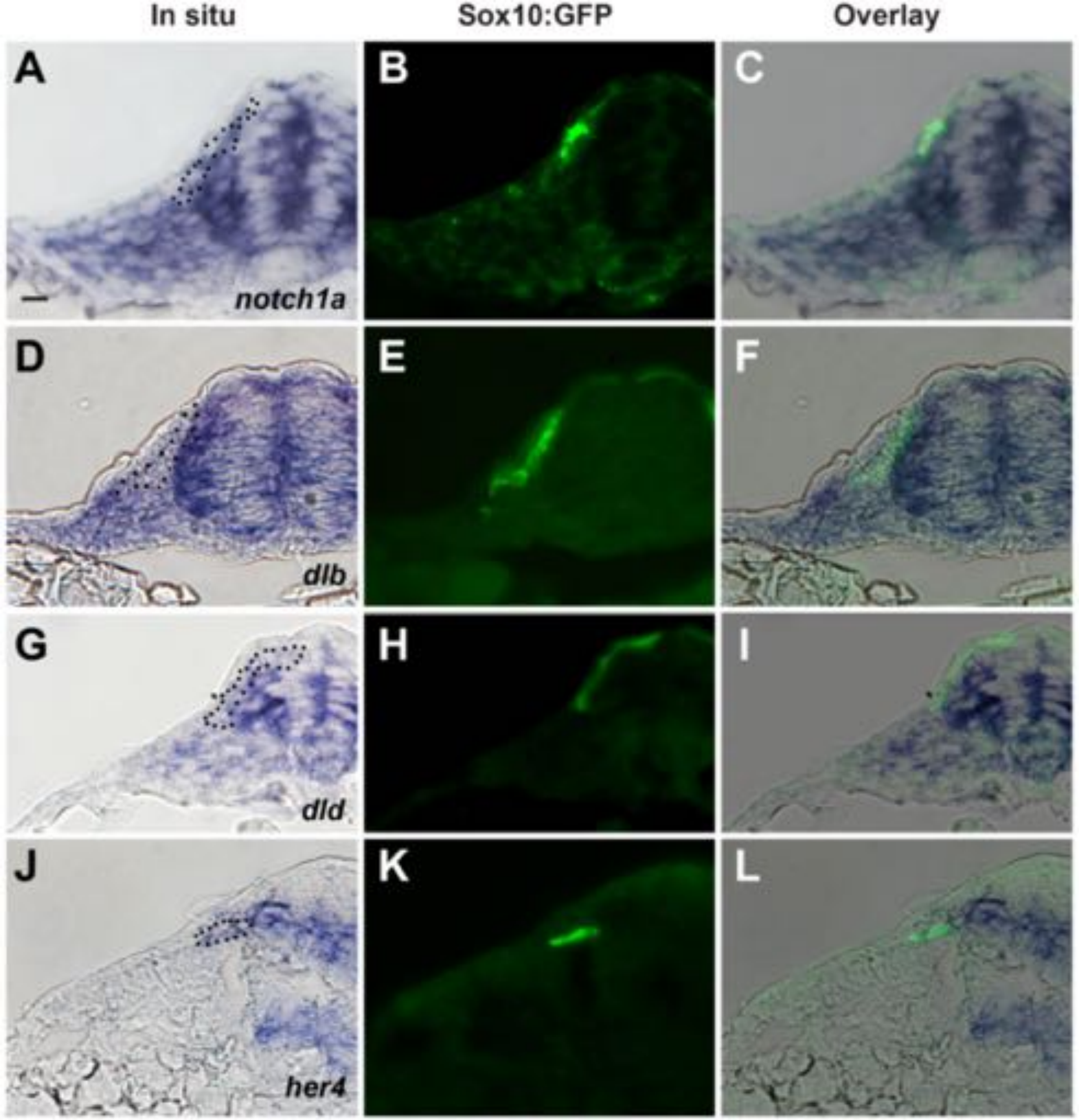
In situ
Sox10:GFP
Overlay
A
B
C
notch1a
D
E
F
dlb
G
H
I
dld
J
K
L
her4

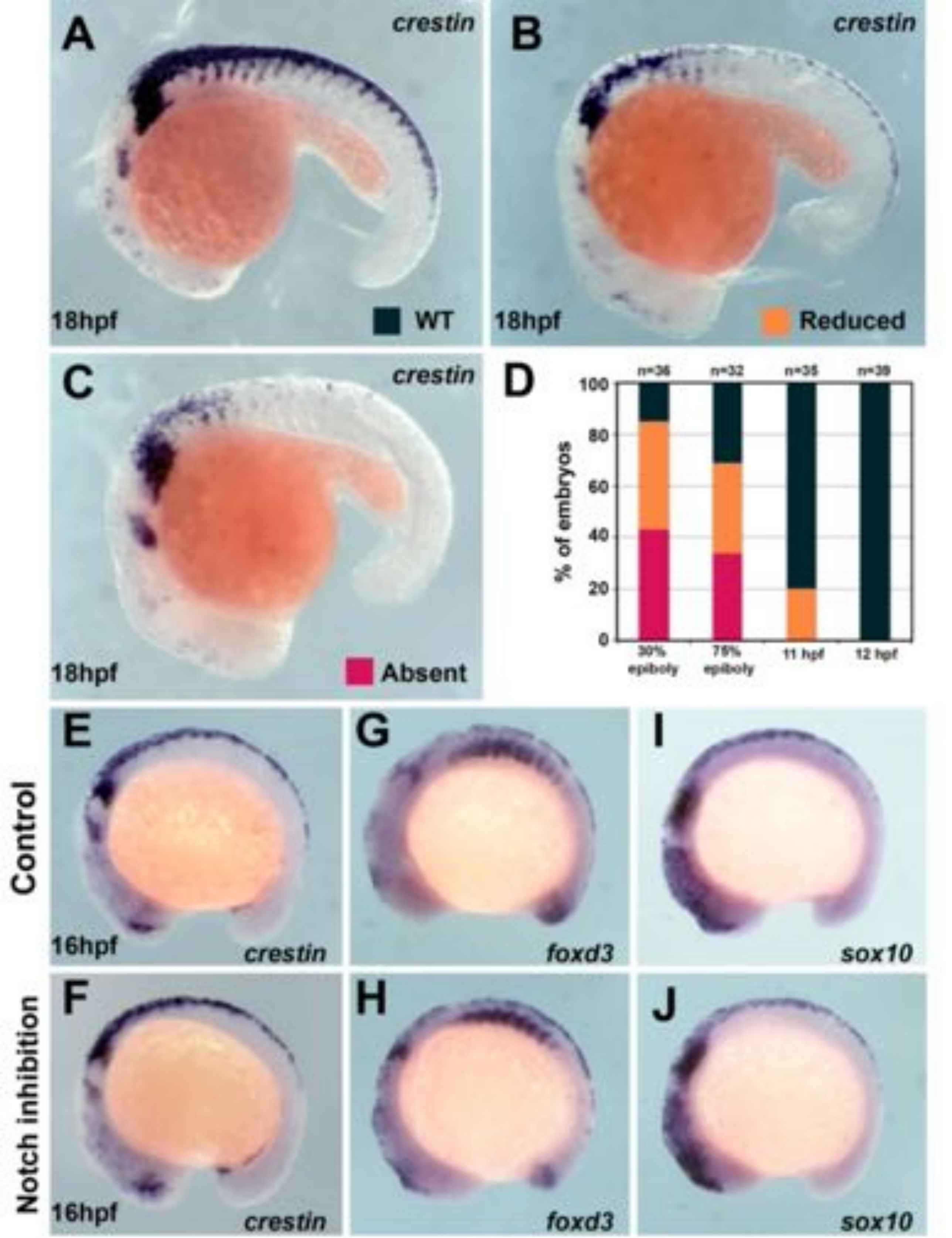
A
crestin
18hpf
WT
B
crestin
18hpf
Reduced
C
crestin
18hpf
Absent
D
n=36
n=32
n=35
n=39
% of embryos
100
80
60
40
20
0
30% epiboly
75% epiboly
11 hpf
12 hpf
Control
Notch inhibition
E
16hpf
crestin
G
foxd3
I
sox10
F
16hpf
crestin
H
foxd3
J
sox10

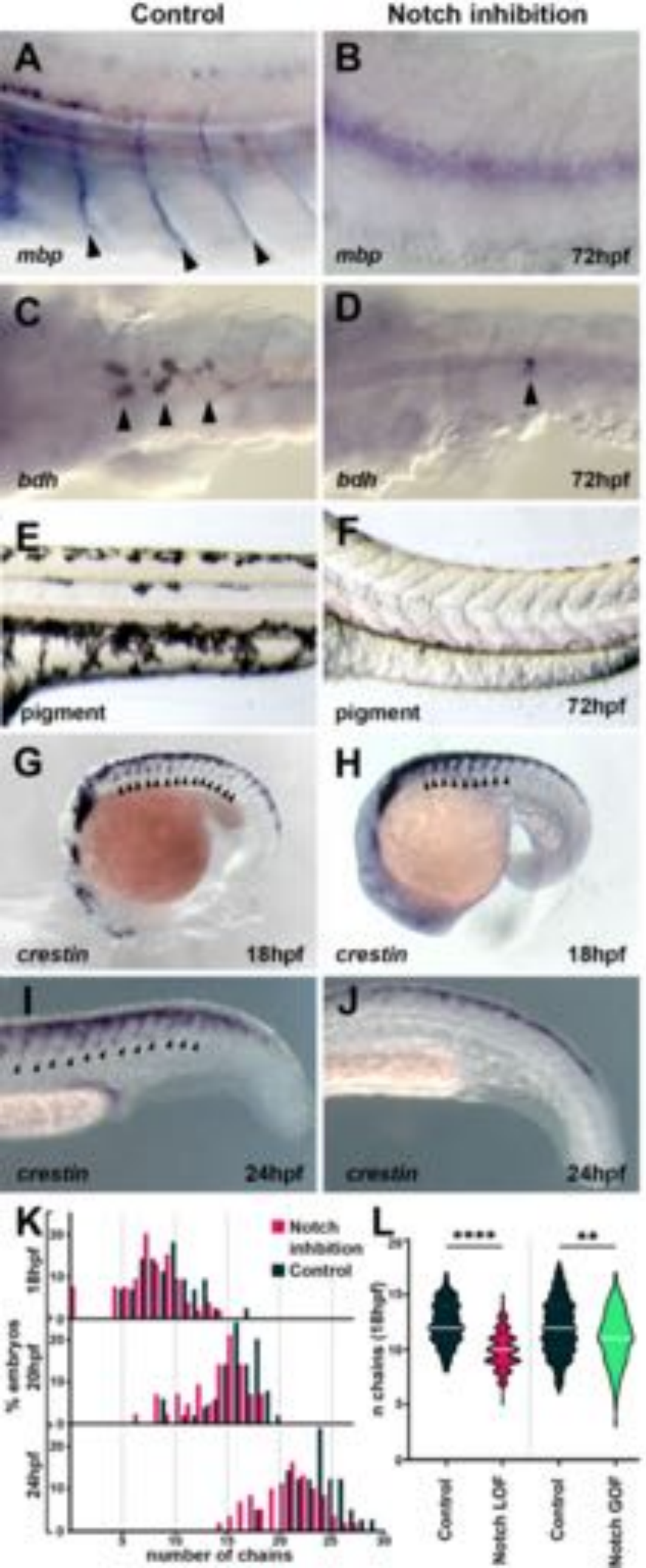
Control
Notch inhibition
A
mbp
B
mbp
72hpf
C
bdh
D
bdh
72hpf
E
pigment
F
pigment
72hpf
G
crestin
18hpf
H
crestin
18hpf
I
crestin
24hpf
J
crestin
24hpf
K
Notch inhibition
Control
% embryos
18hpf
20hpf
24hpf
number of chains
L
****
**
n chains (18hpf)
Control
Notch LOF
Control
Notch GOF

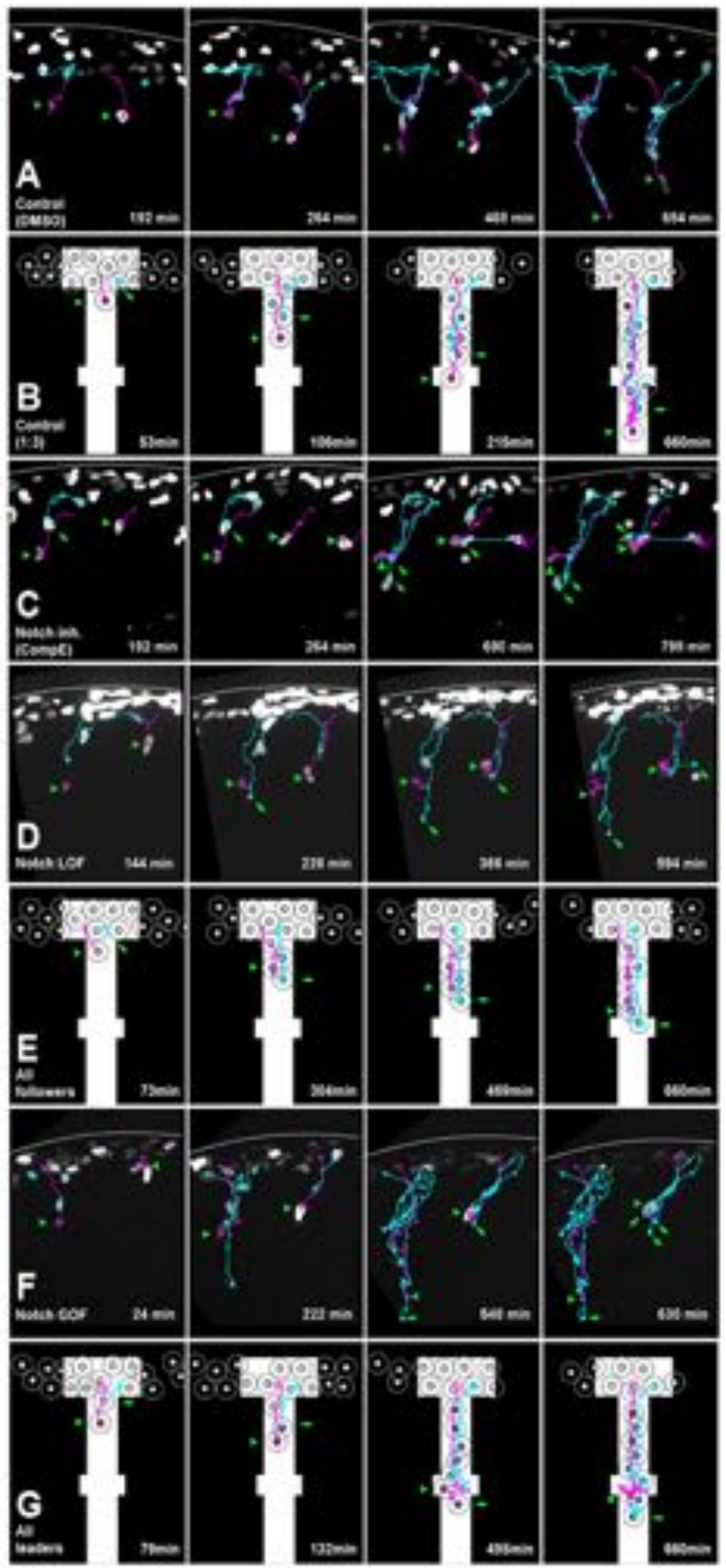
A
Control
(DMSO)
192 min
264 min
468 min
654 min
B
Control
(1:3)
53min
106min
210min
660min
C
Notch inh.
(CompE)
192 min
264 min
690 min
798 min
D
Notch LOF
144 min
228 min
366 min
594 min
E
All
followers
72min
384min
480min
660min
F
Notch GOF
24 min
222 min
648 min
636 min
G
All
leaders
78min
132min
438min
660min

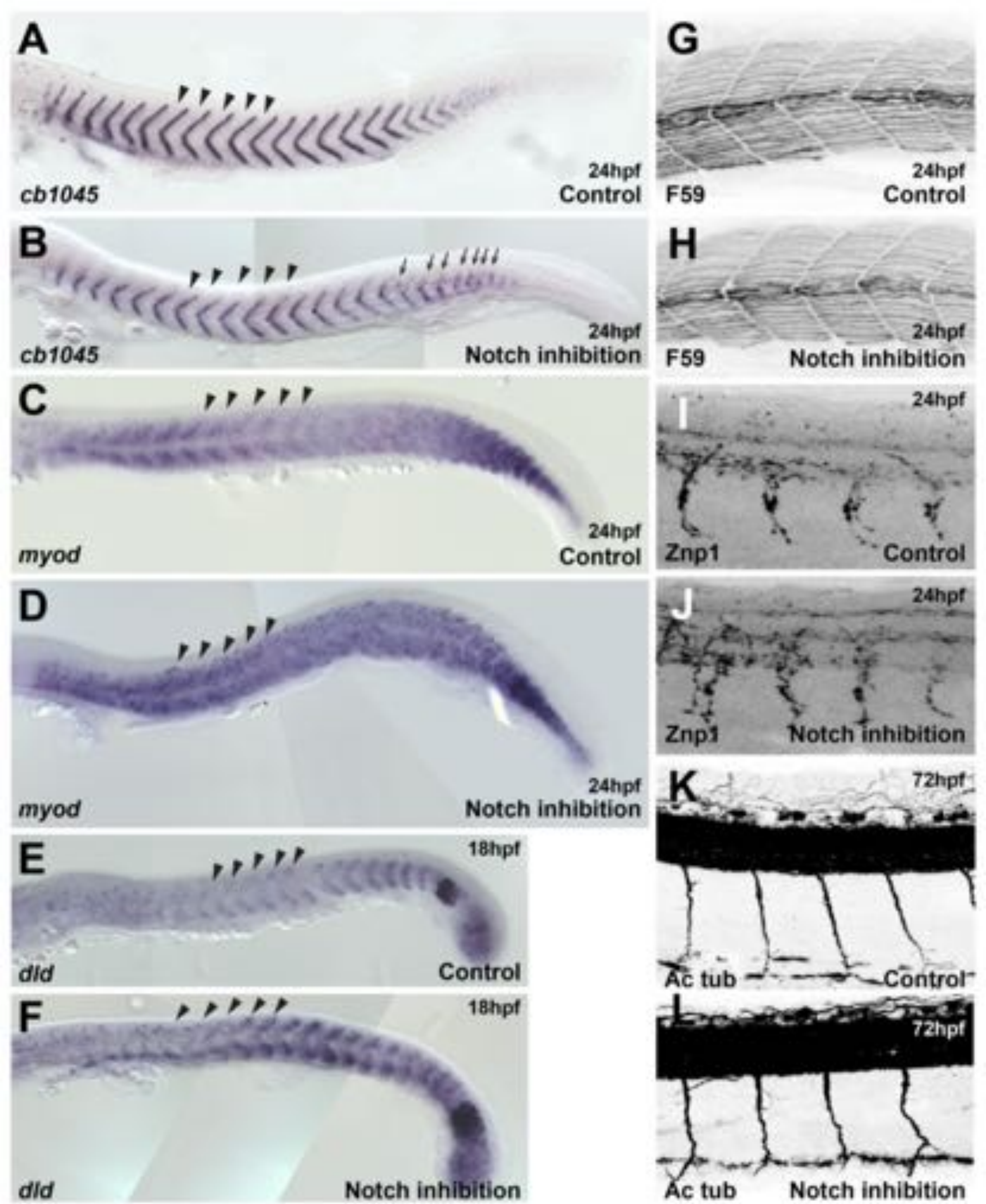
A
cb1045
24hpf
Control
B
cb1045
24hpf
Notch inhibition
C
myod
24hpf
Control
D
myod
24hpf
Notch inhibition
E
dld
18hpf
Control
F
dld
18hpf
Notch inhibition
G
F59
24hpf
Control
H
F59
24hpf
Notch inhibition
I
Znp1
24hpf
Control
J
Znp1
24hpf
Notch inhibition
K
Ac tub
72hpf
Control
L
Ac tub
72hpf
Notch inhibition

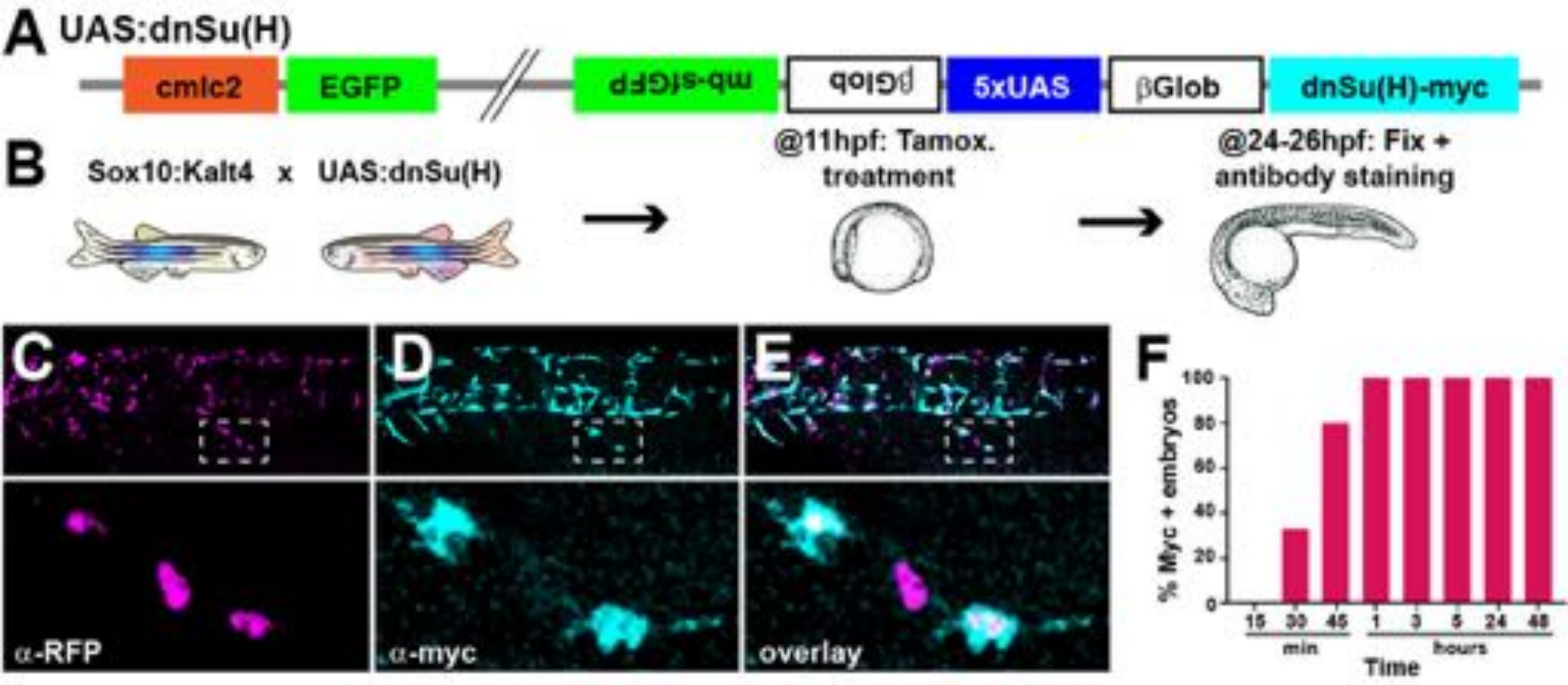
A
UAS:dnSu(H)
cmlc2
EGFP
mb-siGFP
βGlob
5xUAS
βGlob
dnSu(H)-myc
B
Sox10:Kalt4 x UAS:dnSu(H)
@11hpf: Tamox. treatment
@24-26hpf: Fix + antibody staining
C
D
E
α-RFP
α-myc
overlay
F
% Myc + embryos
100
80
60
40
20
0
15
30
45
1
3
5
24
48
min
hours
Time

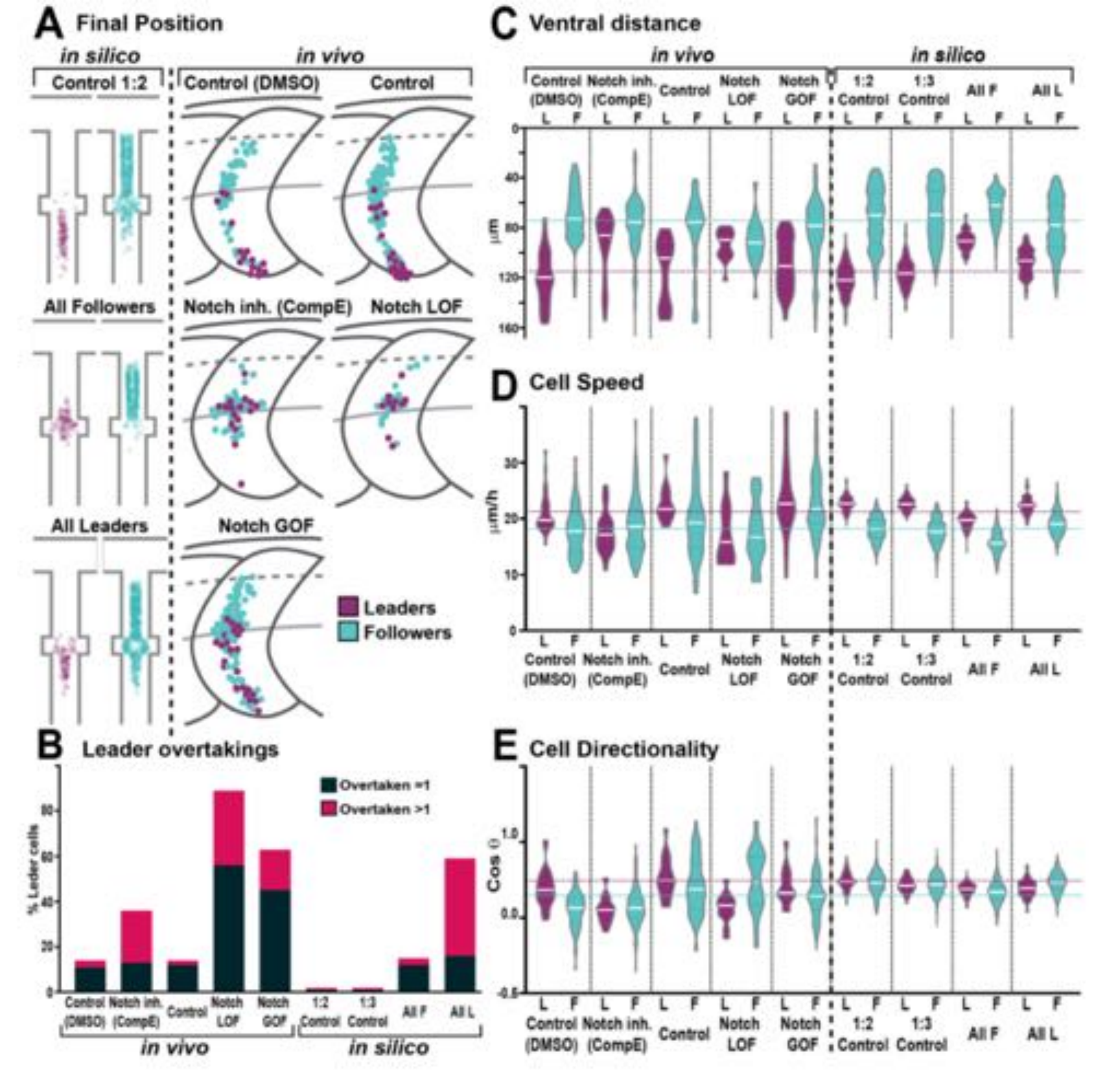
A Final Position
in silico
in vivo
Control 1:2
Control (DMSO)
Control
All Followers
Notch inh. (CompE)
Notch LOF
All Leaders
Notch GOF
Leaders
Followers
B Leader overtakings
Overtaken =1
Overtaken >1
% Leader cells
Control (DMSO)
Notch inh. (CompE)
Control
Notch LOF
Notch GOF
1:2 Control
1:3 Control
All F
All L
in vivo
in silico
C Ventral distance
µm
D Cell Speed
µm/h
E Cell Directionality
Cos (θ)
L
F

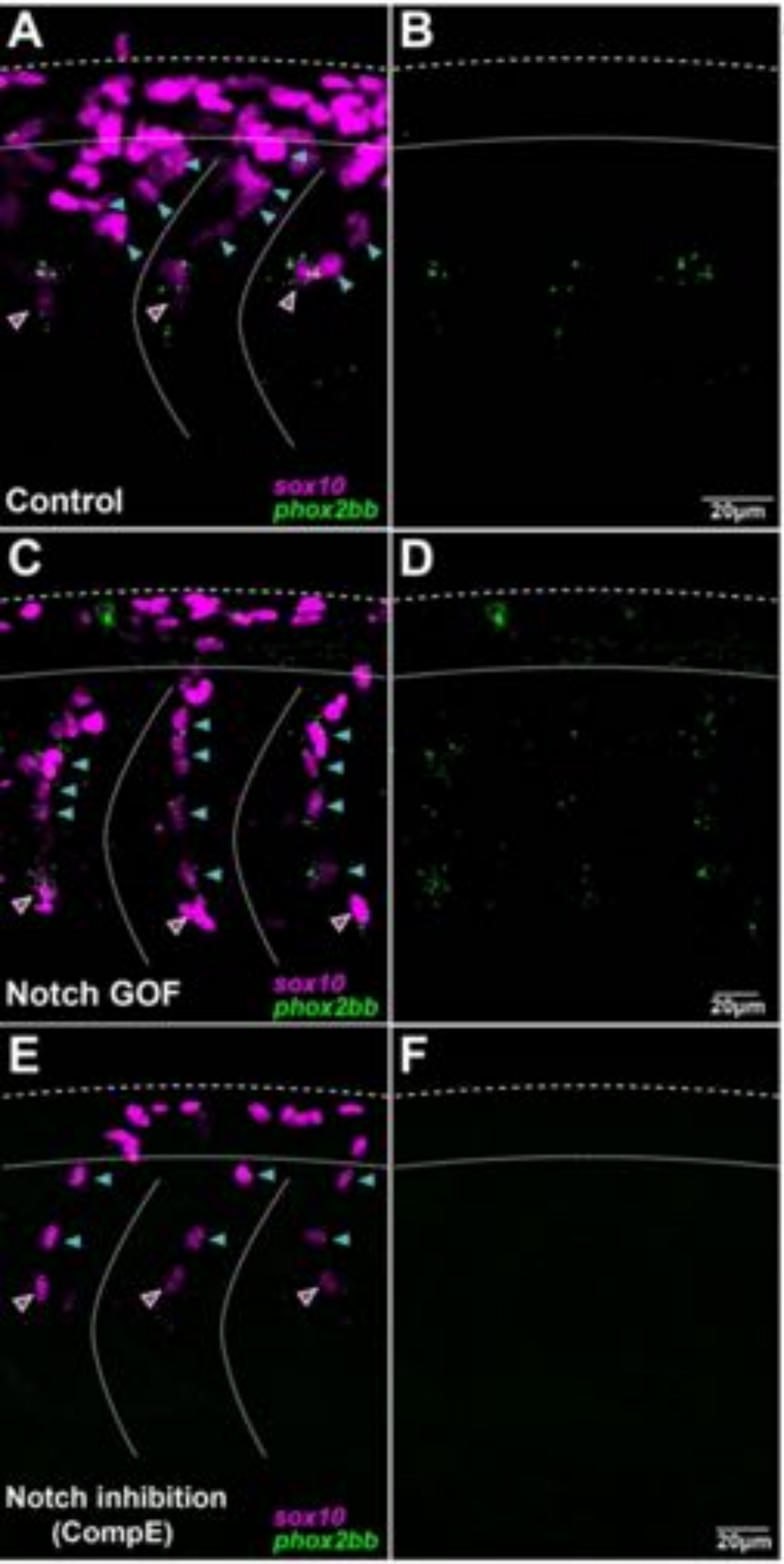
A
B
Control
sox10
phox2bb
20µm
C
D
Notch GOF
sox10
phox2bb
20µm
E
F
Notch inhibition
(CompE)
sox10
phox2bb
20µm

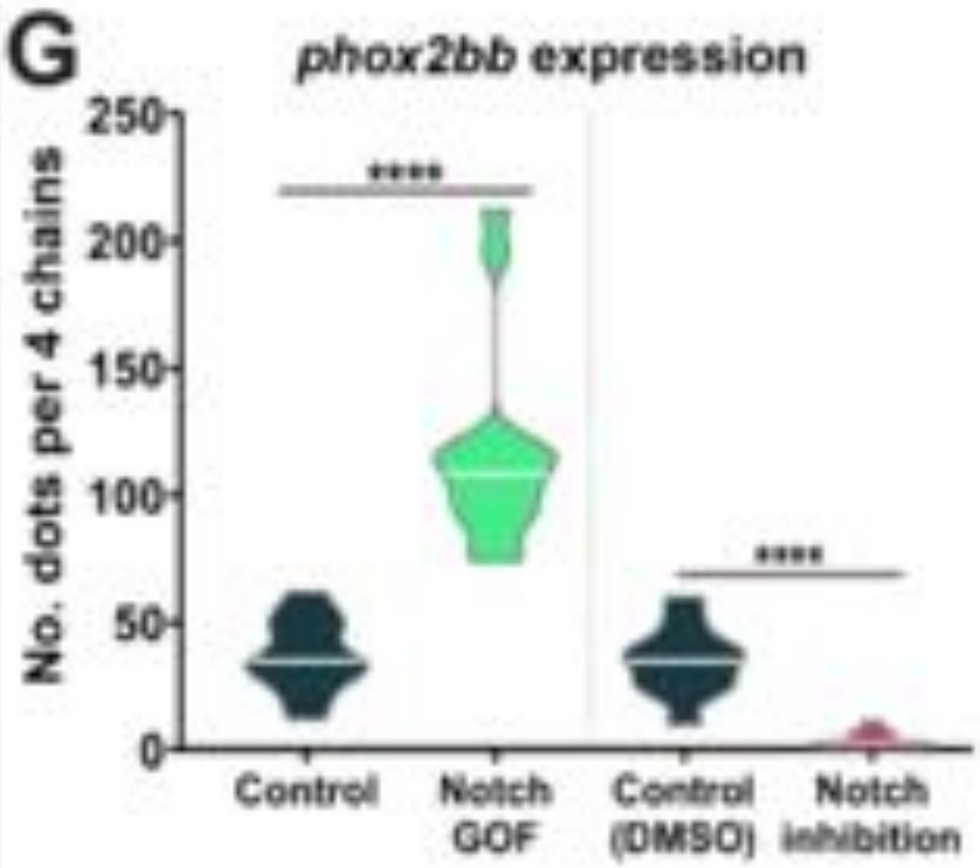
G
phox2bb expression
No. dots per 4 chains
250
200
150
100
50
0
****
****
Control
Notch GOF
Control (DMSO)
Notch inhibition

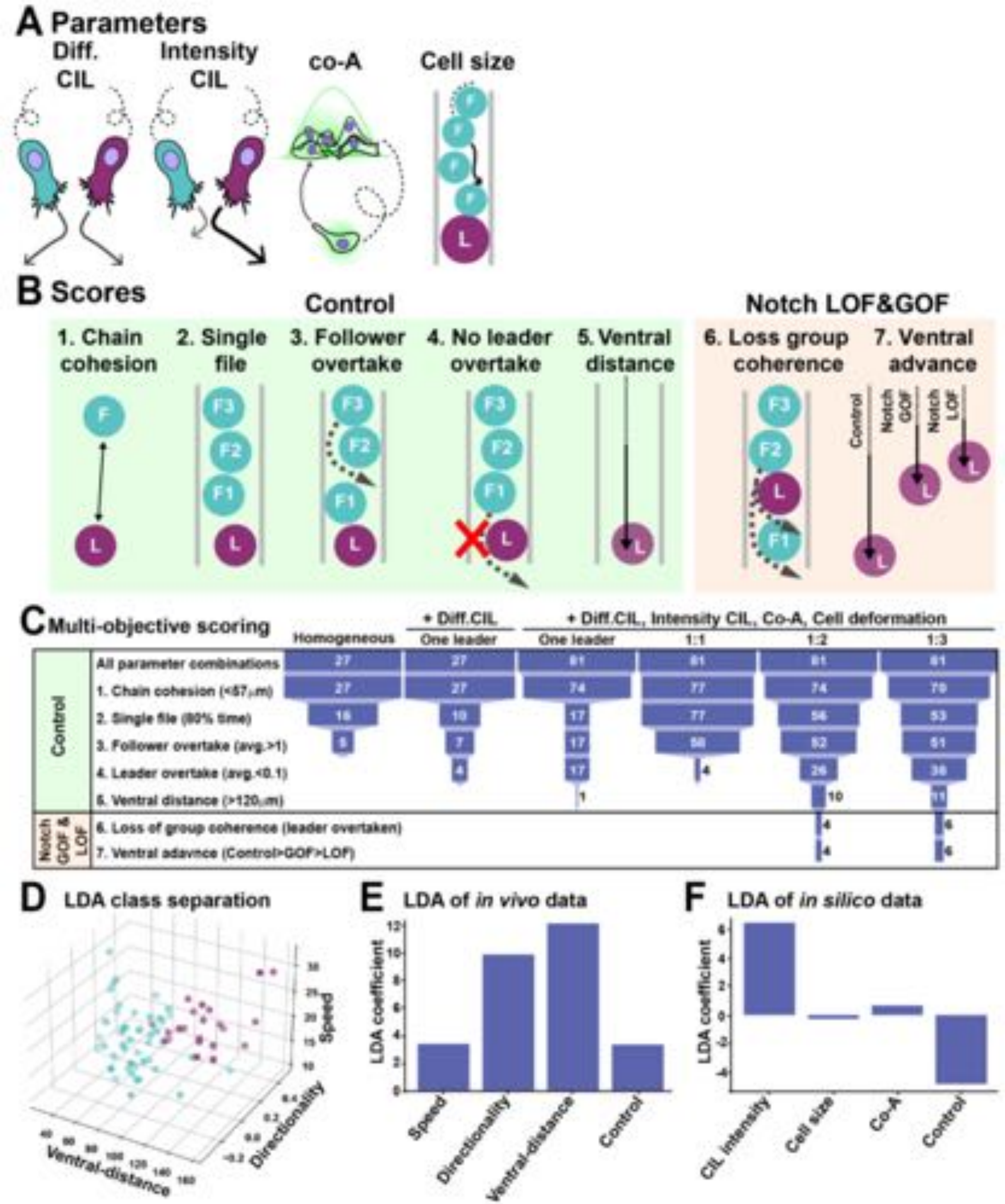
A Parameters
Diff. CIL
Intensity CIL
co-A
Cell size
B Scores
Control
Notch LOF&GOF
1. Chain cohesion
2. Single file
3. Follower overtake
4. No leader overtake
5. Ventral distance
6. Loss group coherence
7. Ventral advance
Control
Notch GOF
Notch LOF
C Multi-objective scoring
+ Diff.CIL
+ Diff.CIL, Intensity CIL, Co-A, Cell deformation
Homogeneous
One leader
One leader
1:1
1:2
1:3
All parameter combinations
1. Chain cohesion (<57μm)
2. Single file (80% time)
3. Follower overtake (avg.>1)
4. Leader overtake (avg.<0.1)
5. Ventral distance (>120μm)
6. Loss of group coherence (leader overtaken)
7. Ventral adavnce (Control>GOF>LOF)
Notch GOF & LOF
D LDA class separation
Speed
Directionality
Ventral-distance
E LDA of in vivo data
LDA coefficient
Speed
Directionality
Ventral-distance
Control
F LDA of in silico data
LDA coefficient
CIL intensity
Cell size
Co-A
Control

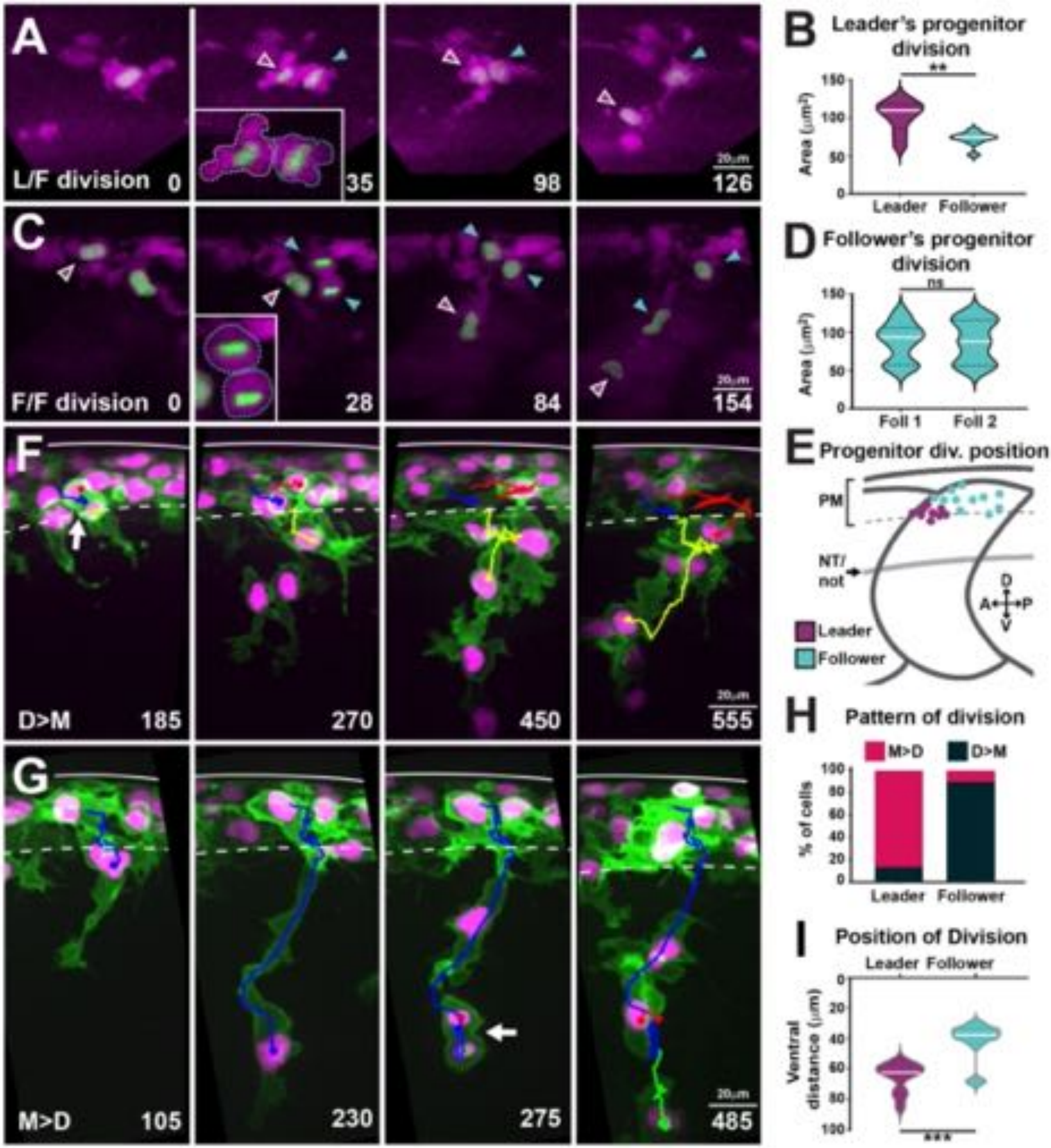
A
L/F division
0
35
98
126
20µm
B
Leader's progenitor division
**
Area (µm²)
150
100
50
0
Leader
Follower
C
F/F division
0
28
84
154
20µm
D
Follower's progenitor division
ns
Area (µm²)
150
100
50
0
Foll 1
Foll 2
E
Progenitor div. position
PM
NT/
not
D
A
P
V
Leader
Follower
F
D>M
185
270
450
555
20µm
H
Pattern of division
M>D
D>M
% of cells
100
80
60
40
20
0
Leader
Follower
G
M>D
105
230
275
485
20µm
I
Position of Division
Leader
Follower
Ventral distance (µm)
0
20
40
60
80
100
***

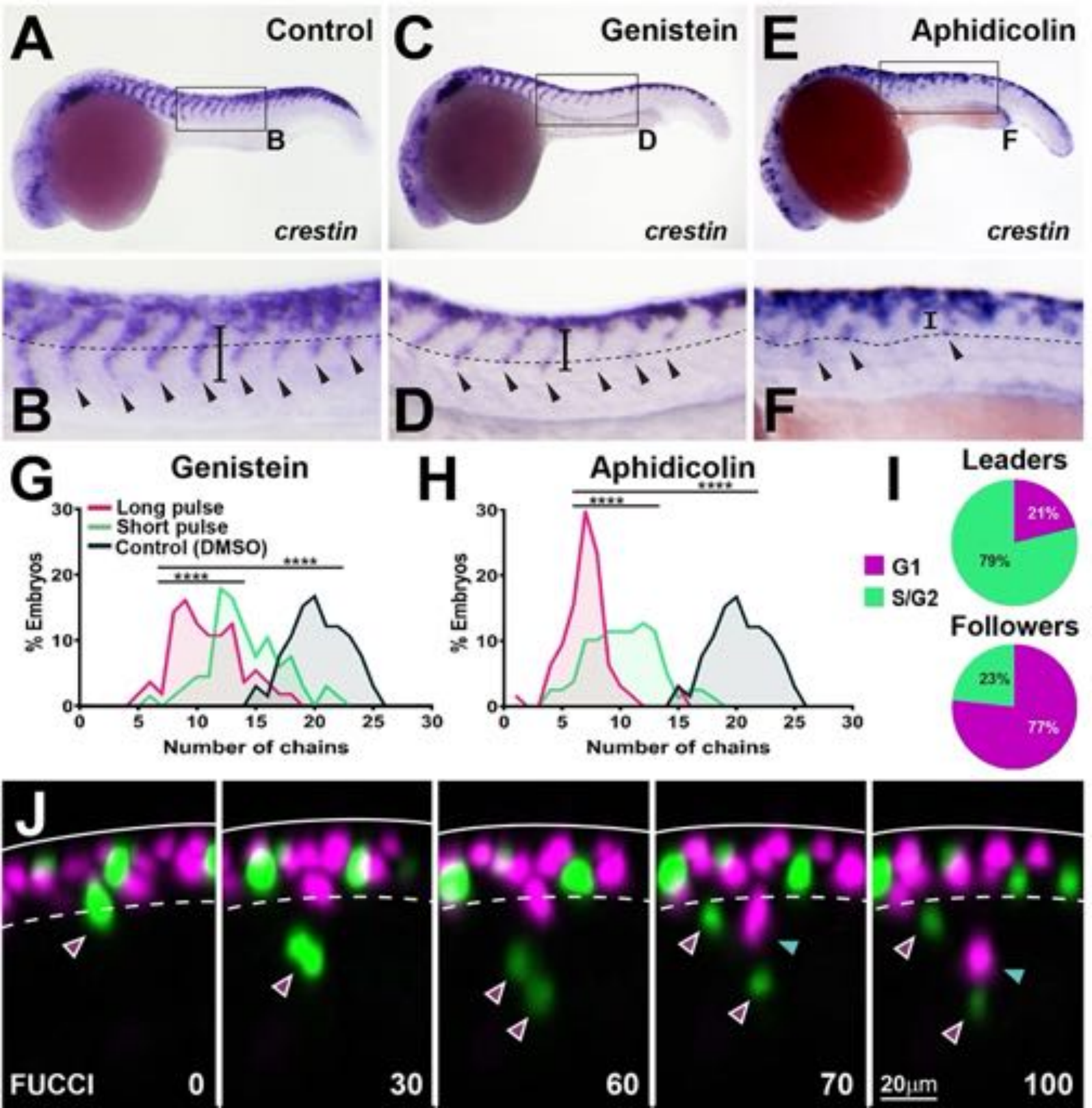
A
Control
B
crestin
C
Genistein
D
crestin
E
Aphidicolin
F
crestin
B
D
F
G
Genistein
Long pulse
Short pulse
Control (DMSO)
****
****
% Embryos
Number of chains
H
Aphidicolin
****
****
% Embryos
Number of chains
I
Leaders
21%
79%
G1
S/G2
Followers
23%
77%
J
FUCCI
0
30
60
70
20µm
100

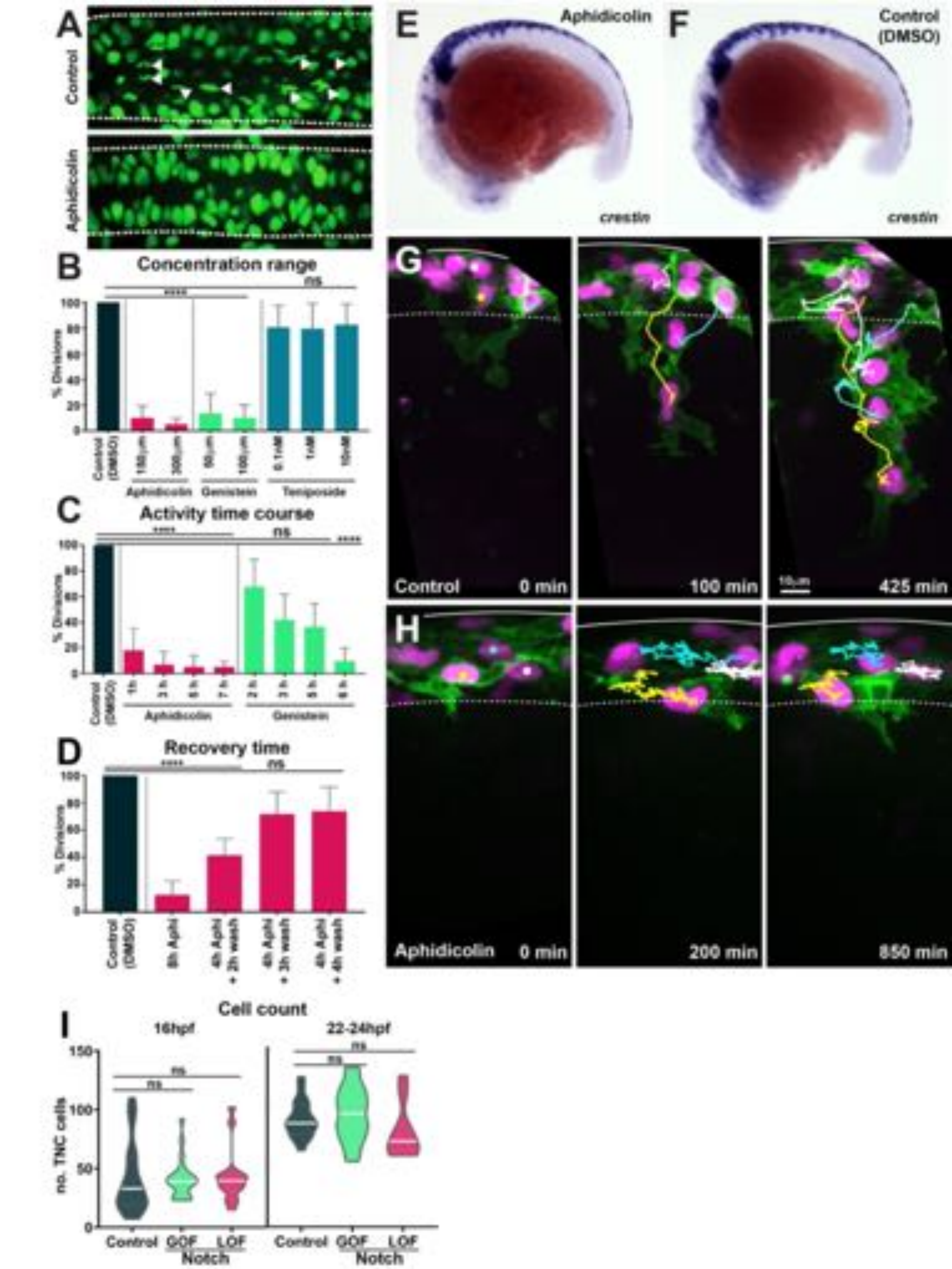
A
Control
Aphidicolin
B
Concentration range
ns
% Divisions
Control (DMSO)
Aphidicolin
Genistein
Teniposide
C
Activity time course
ns
Aphidicolin
Genistein
D
Recovery time
ns
% Divisions
Control (DMSO)
4h Aphi
4h Aphi 2h wash
4h Aphi 3h wash
4h Aphi 4h wash
E
Aphidicolin
crestin
F
Control (DMSO)
crestin
G
Control
0 min
100 min
425 min
H
Aphidicolin
0 min
200 min
850 min
I
Cell count
16hpf
22-24hpf
ns
no. TNC cells
Control
GOF
LOF
Notch

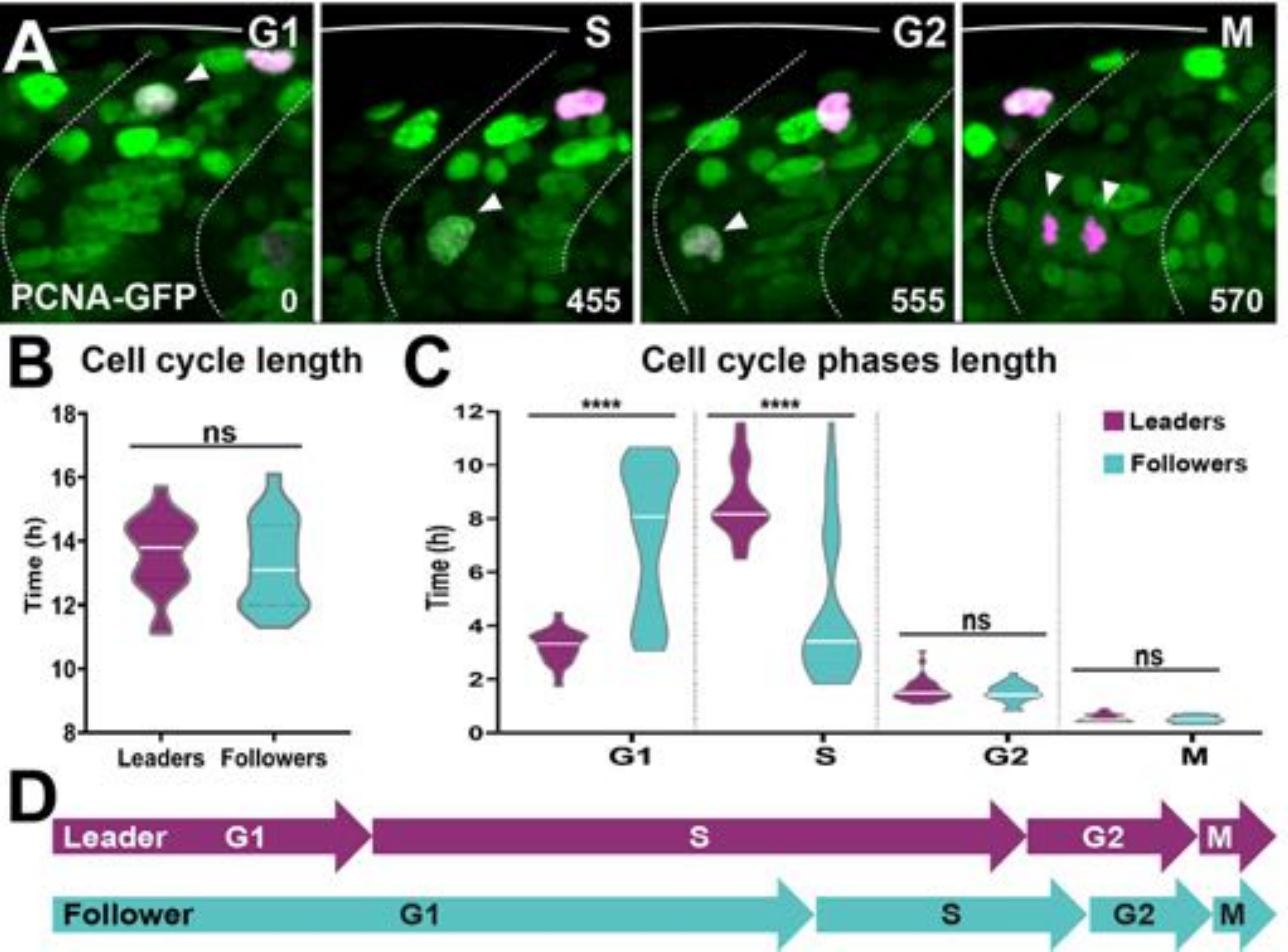
A
G1
S
G2
M
PCNA-GFP
0
455
555
570
B
Cell cycle length
ns
Time (h)
18
16
14
12
10
8
Leaders
Followers
C
Cell cycle phases length
****
****
ns
ns
Time (h)
12
10
8
6
4
2
0
G1
S
G2
M
Leaders
Followers
D
Leader
G1
S
G2
M
Follower
G1
S
G2
M

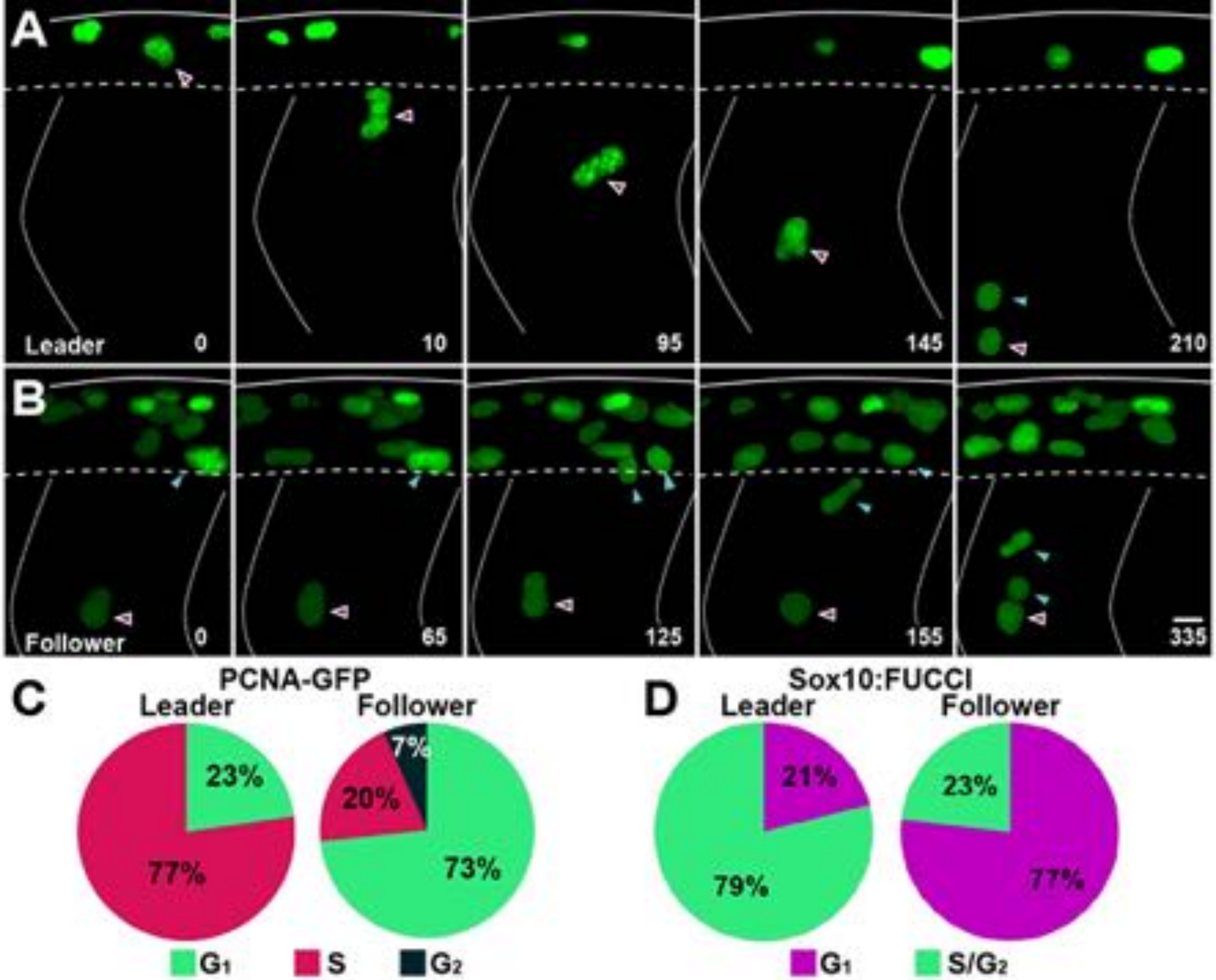
A
Leader
0
10
95
145
210
B
Follower
0
65
125
155
335
C
PCNA-GFP
Leader
Follower
23%
77%
7%
20%
73%
G1
S
G2
D
Sox10:FUCCI
Leader
Follower
21%
79%
23%
77%
G1
S/G2

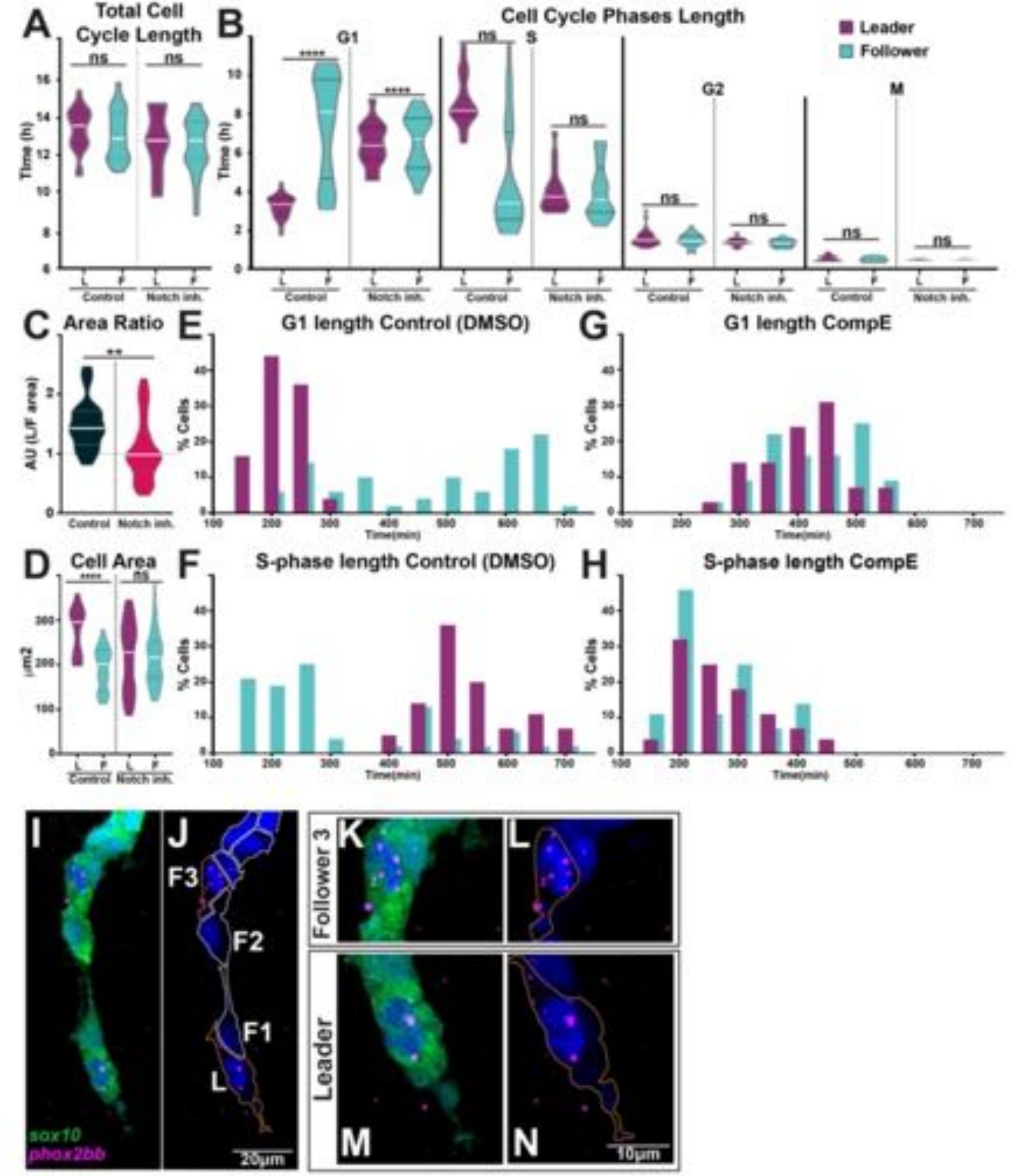
A
Total Cell Cycle Length
Time (h)
ns
ns
Control
Notch inh.
B
Cell Cycle Phases Length
Leader
Follower
G1
S
G2
M
****
****
ns
ns
ns
ns
ns
Time (h)
Control
Notch inh.
C
Area Ratio
AU (L/F area)
**
Control
Notch inh.
D
Cell Area
µm2
****
ns
Control
Notch inh.
E
G1 length Control (DMSO)
% Cells
Time(min)
F
S-phase length Control (DMSO)
% Cells
Time(min)
G
G1 length CompE
% Cells
Time(min)
H
S-phase length CompE
% Cells
Time(min)
I
sox10
phox2bb
J
F3
F2
F1
L
20µm
Follower 3
K
L
Leader
M
N
10µm

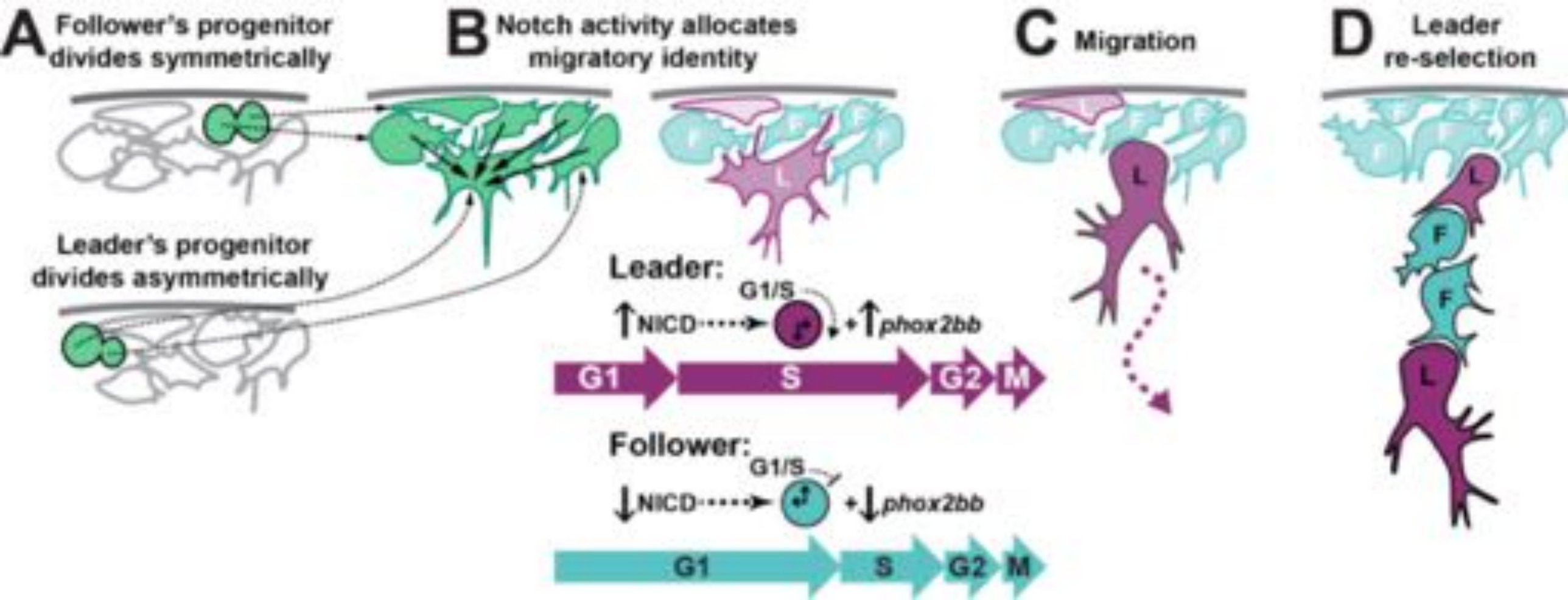
A Follower's progenitor divides symmetrically
B Notch activity allocates migratory identity
C Migration
D Leader re-selection
Leader's progenitor divides asymmetrically
Leader:
G1/S
↑NICD
+↑phox2bb
G1
S
G2
M
Follower:
G1/S
↓NICD
+↓phox2bb
G1
S
G2
M
L
F

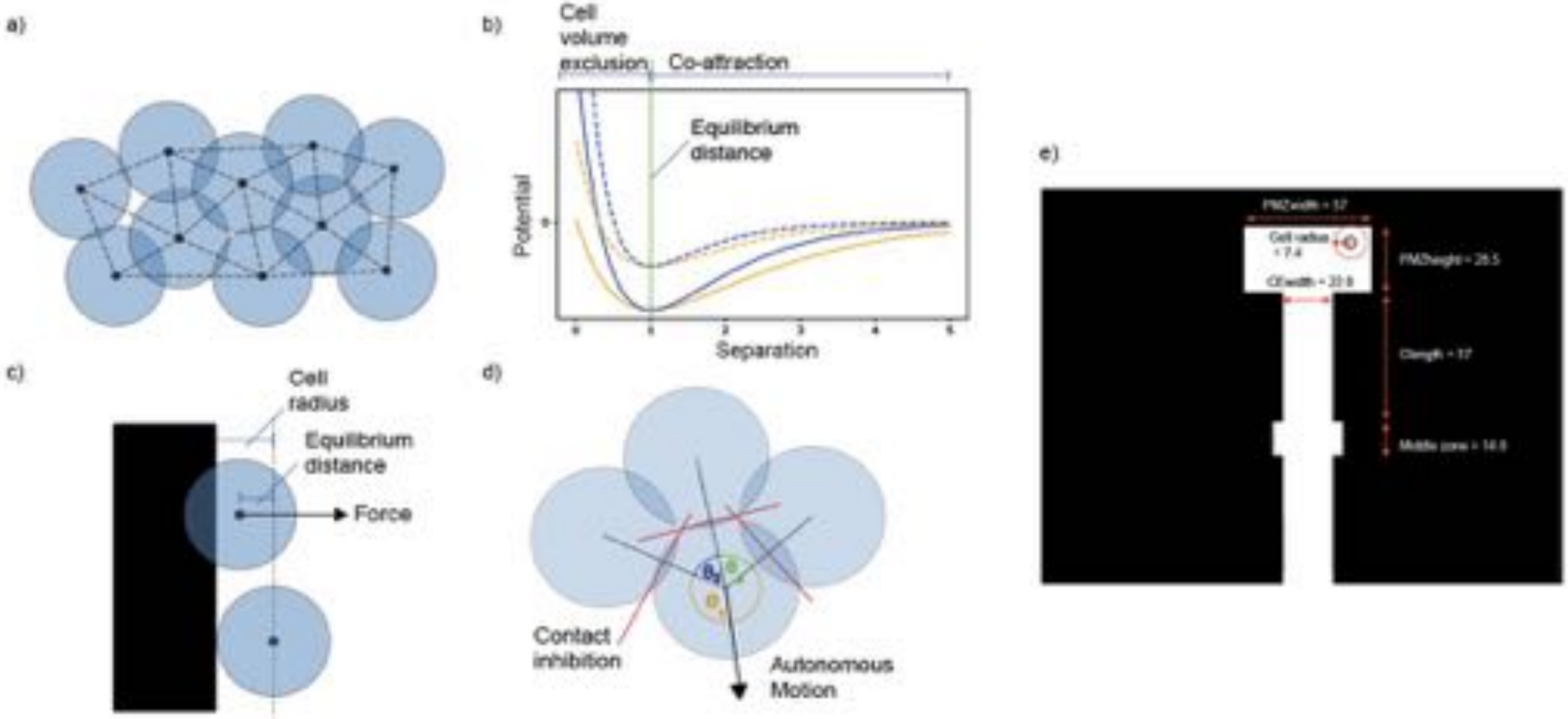
a)
b)
Cell volume exclusion
Co-attraction
Equilibrium distance
Potential
Separation
c)
Cell radius
Equilibrium distance
Force
d)
Contact inhibition
Autonomous Motion
e)

1. Initialise cells within the PMZ

2. Loop until maximum time has been reached:

    2.1. Perform Delaunay triangulation on cells

    2.2. Identify neighbours

    2.3. Calculate forces between nearest neighbours

    2.4. Apply boundary forces to all cells

    2.5. Calculate autonomous motion velocities as determined by contact inhibition

    2.6. Calculate noise

    2.7. Update system

    2.8. Apply experimental conditions for the next time step

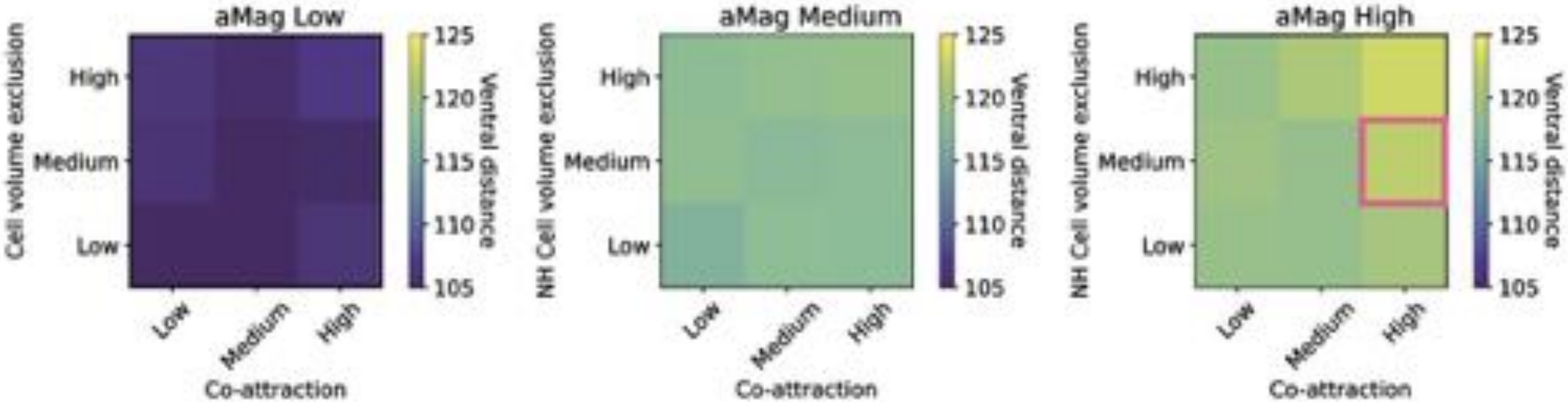
aMag Low
aMag Medium
aMag High
Cell volume exclusion
NH Cell volume exclusion
High
Medium
Low
Co-attraction
Ventral distance
125
120
115
110
105